Atmospheric Conditions during the Deep Propagating Gravity Wave Experiment (DEEPWAVE)

SONJA GISINGER,[a] ANDREAS DÖRNBRACK,[a] VIVIEN MATTHIAS,[b] JAMES D. DOYLE,[c] STEPHEN D. ECKERMANN,[d] BENEDIKT EHARD,[a] LARS HOFFMANN,[e] BERND KAIFLER,[a] CHRISTOPHER G. KRUSE,[f] AND MARKUS RAPP[a,g]

[a] *Deutsches Zentrum für Luft- und Raumfahrt, Institut für Physik der Atmosphäre, Oberpfaffenhofen, Germany*
[b] *Leibniz Institute of Atmospheric Physics, University of Rostock, Kühlungsborn, Germany*
[c] *Marine Meteorology Division, U.S. Naval Research Laboratory, Monterey, California*
[d] *Space Science Division, U.S. Naval Research Laboratory, Washington, D.C.*
[e] *Jülich Supercomputing Centre, Forschungszentrum Jülich, Jülich, Germany*
[f] *Department of Geology and Geophysics, Yale University, New Haven, Connecticut*
[g] *Meteorologisches Institut München, Ludwig-Maximilians-Universität, Munich, Germany*

(Manuscript received 18 November 2016, in final form 9 June 2017)

ABSTRACT

This paper describes the results of a comprehensive analysis of the atmospheric conditions during the Deep Propagating Gravity Wave Experiment (DEEPWAVE) campaign in austral winter 2014. Different datasets and diagnostics are combined to characterize the background atmosphere from the troposphere to the upper mesosphere. How weather regimes and the atmospheric state compare to climatological conditions is reported upon and how they relate to the airborne and ground-based gravity wave observations is also explored. Key results of this study are the dominance of tropospheric blocking situations and low-level southwesterly flows over New Zealand during June–August 2014. A varying tropopause inversion layer was found to be connected to varying vertical energy fluxes and is, therefore, an important feature with respect to wave reflection. The subtropical jet was frequently diverted south from its climatological position at 30°S and was most often involved in strong forcing events of mountain waves at the Southern Alps. The polar front jet was typically responsible for moderate and weak tropospheric forcing of mountain waves. The stratospheric planetary wave activity amplified in July leading to a displacement of the Antarctic polar vortex. This reduced the stratospheric wind minimum by about 10 m s^{-1} above New Zealand making breaking of large-amplitude gravity waves more likely. Satellite observations in the upper stratosphere revealed that orographic gravity wave variances for 2014 were largest in May–July (i.e., the period of the DEEPWAVE field phase).

1. Introduction

The overarching objectives of the Deep Propagating Gravity Wave Experiment (DEEPWAVE; see appendix A for a list of key acronyms used in this paper) were to observe, model, understand, and predict the deep vertical propagation of internal gravity waves from the troposphere to the lower thermosphere and to study their impacts on the atmospheric momentum and energy budget (Fritts et al. 2016). Convection, fronts, flow over mountains, and spontaneous adjustments occurring at the tropospheric jet streams generate vertically propagating gravity waves in the troposphere and lower stratosphere (Smith 1979; Gill 1982; Baines 1995; Fritts and Alexander 2003; Nappo 2012; Sutherland 2010; Plougonven and Zhang 2014). Through their far-field interactions, gravity waves constitute an important coupling mechanism in Earth's atmosphere. The associated redistribution of momentum and energy controls the global middle-atmospheric circulation (Dunkerton 1978; Lindzen 1981).

To investigate the different sources of gravity waves under favorable atmospheric conditions for deep vertical propagation, a climatological local maximum in gravity wave (GW) activity (a so-called hotspot) was sought in the Southern Hemisphere (SH) during austral winter. Besides the southern Andes, the Antarctic Peninsula, Tasmania, and other small islands in the Southern Ocean, the South Island (SI) of New Zealand constitutes one of several hotspots of stratospheric

Corresponding author: Sonja Gisinger, sonja.gisinger@dlr.de

DOI: 10.1175/MWR-D-16-0435.1

gravity wave activity in the Southern Hemisphere during austral winter (e.g., Jiang et al. 2006; Hoffmann et al. 2016). The SI represents an isolated barrier for westerly and northwesterly winds and its location is close to the polar front and subtropical jet streams, which in the following are denoted by PFJ and STJ, respectively. Furthermore, the SI's geographical location at about 45°S ensures proximity to the stratospheric polar night jet (PNJ), a flow environment that should enable deep vertical propagation of gravity waves excited by the flow across the Southern Alps of the SI. Therefore, and for further reasons discussed in Fritts et al. (2016), the SI was chosen as the operating base for the experiment.

The mission targets defined prior to the field phase were inter alia based on a detailed appraisal of waves in model and satellite climatologies as well as experience derived from a "dry run" of the field experiment conducted the year before DEEPWAVE (Fritts et al. 2016). Specific deep-propagating gravity wave targets were

- orographic and trailing waves (Fritts et al. 2016) in the vicinity of the SI,
- orographic and trailing waves in the vicinity of Tasmania,
- orographic and nonorographic waves in the vicinity of the Auckland Islands (Pautet et al. 2016; Eckermann et al. 2016) and Macquarie Island, and
- nonorographic waves over the southern Pacific Ocean forced by jet streams, fronts, convection, and other sources, and
- predictability and targeting missions to sample regions of initial sensitivity to orographic wave forcing over SI, typically located upstream of New Zealand.

Altogether, the DEEPWAVE area of operations encompassed a region from 65° to 30°S and from 145°E to 180°. The field phase of DEEPWAVE was conducted during May–July 2014. Measurements taken on board the two research aircraft, the NSF/NCAR GV and the DLR Falcon, provided gravity wave data from the lower troposphere to the mesosphere using a variety of in situ and remote sensing instruments (Fritts et al. 2016). The aircraft measurements were complemented by radiosonde soundings and ground-based measurements at various locations distributed over the SI, Tasmania, and Macquarie Island: for example, by a tropospheric UHF wind profiler, an airglow imager, a mesospheric temperature mapper, a Rayleigh lidar, and a meteor radar [see Fig. 1 in Fritts et al. (2016)]. The Rayleigh lidar measurements at Lauder, New Zealand (45.0°S, 169.7°E), were continued until early November 2014 (Kaifler et al. 2015, 2017).

The present paper analyzes the atmospheric conditions from the troposphere up to the mesosphere during austral winter 2014. We emphasize key circulation features during the DEEPWAVE campaign period and relate them to the climatological mean conditions. The different meteorological conditions are related to observed wave events [intensive observing periods (IOPs) with airborne observations and periods with only ground-based (GB) measurements as listed in Tables 4 and 5 in Fritts et al. (2016)]. Section 2 provides information about the various datasets used in this study. In section 3, we discuss specific tropospheric flow regimes and forcing conditions during DEEPWAVE. Section 4 is devoted to the tropopause layer. The stratospheric and mesospheric wind and thermal conditions providing the ambient atmospheric profiles for deep propagating gravity waves are described in section 5. There, planetary wave activity and its impact on the location of the PNJ and the polar vortex are discussed. Special attention is paid to the wind and temperature conditions above 60-km altitude using the recently published reanalyses of the Navy Global Environmental Model (NAVGEM; Eckermann et al. 2016) extending up to 100 km. In section 6, we discuss satellite observations of gravity waves at around 40-km altitude over the SI of New Zealand. Section 7 summarizes the major findings of the paper, which will serve as a reference for future scientific investigations of gravity wave observations acquired during DEEPWAVE.

2. Data sources

Operational analyses of the Integrated Forecast System (IFS) of the European Centre for Medium-Range Weather Forecasts (ECMWF) are used to provide meteorological data to characterize the atmospheric situation. The 6-hourly operational analysis and hourly forecast fields of the IFS cycle 40r1 have a horizontal resolution on the reduced linear Gaussian grid of about 16 km (T_L1279) and 137 vertical model levels (L137) from the ground to ~80 km (0.01 hPa) with layer thicknesses gradually increasing from ~300 m at ~10-km altitude to ~400 m at ~20-km altitude and ~2 km at ~60-km altitude. Analyzed IFS winds are assumed to be reliable up to ~60-km altitude [Le Pichon et al. (2015): see also material presented in appendix B]. Additionally, ERA-Interim (Dee et al. 2011) and NCEP–NCAR (Kalnay et al. 1996) reanalysis data are used to calculate climatological indices and anomalies of the horizontal wind and geopotential height on selected pressure surfaces.

In addition to these operational analyses, a reanalysis of the 2014 DEEPWAVE austral winter was performed using a high-altitude research version of the NAVGEM system (Hogan et al. 2014). The reanalysis discussed here used a T119L74 forecast model and a T47L74

tangent linear model utilizing a four-dimensional variational data assimilation (4DVAR) algorithm in which 80-member forecast ensembles helped to define background error covariances for the analysis (so-called hybrid-4DVAR). The L74 levels have a top full model layer at $\sim 10^{-4}$ hPa. Layer thicknesses increase from ~1 km at 10-km altitude to ~2 km at 40-km altitude, ~3 km at 80-km altitude, and ~4.5 km at ~100-km altitude. Above 50-km altitude the system assimilated limb temperature retrievals from the Microwave Limb Sounder (MLS) and the Sounding of the Atmosphere Using Broadband Emission Radiometry (SABER) on NASA's *Aura* and Thermosphere, Ionosphere, Mesosphere Energetics and Dynamics (TIMED) satellites, respectively, and microwave radiances from the Special Sensor Microwave Imager/Sounder (SSMIS) on operational Defense Meteorological Satellite Program (DMSP) platforms. Additional details are provided in section 2b in Eckermann et al. (2016).

For estimating the planetary wave activity in the stratosphere and mesosphere, temperature and geopotential height from the MLS are analyzed (Waters et al. 2006; Livesey et al. 2017). MLS covers Earth's atmosphere from 82°S to 82°N on each sun-ynchronous sorbit and the data are analyzed between approximately 9 and 97 km (261–0.001 hPa) with a vertical resolution of about 4 km in the stratosphere and about 14 km near the mesopause. The temporal resolution is 1 day at each location and data are available from August 2004 (Livesey et al. 2017). Note that version 4 MLS data are used and that the most recent recommended quality screening procedures of Livesey et al. (2017) have been applied. The two-dimensional least squares method used by Wu et al. (1995) is applied to the global datasets of ERA-Interim and MLS to obtain the quasi-stationary PW1 amplitude. Note that this analysis is done by using a 10-day window shifted by 1 day to eliminate the influence of migrating waves such as tides.

Vertical energy fluxes ($EF_z = \overline{p'w'}$) over the SI at 4- and 12-km altitude were computed from mesoscale simulations of the Weather Research and Forecasting (WRF) Model with a horizontal resolution of 6 km. The model was initialized and continuously guided by MERRA2 reanalyses. To compute the perturbations of pressure and vertical velocity required to compute the EF_z, the fields were high-pass filtered with a cutoff length scale of $L = 400$ km, retaining scales smaller than L. For more details about the energy flux calculations, see Kruse and Smith (2015).

Satellite instruments have often been used to identify so-called hotspots of stratospheric gravity wave activity on a global scale (e.g., Hoffmann et al. 2013). Here, nadir-scanning observations of AIRS (Aumann et al. 2003; Chahine et al. 2006) on board NASA's *Aqua* satellite are used to infer the fraction of orographic waves visible to the instrument over New Zealand. The analysis is based on a 12-yr record (January 2003–December 2014) of 4.3-μm radiance observations of AIRS. Stratospheric gravity wave signals in terms of brightness temperature perturbations and variances are extracted. The analysis procedure is described in detail in Hoffmann et al. (2016). It must be mentioned that the nadir measurement geometry limits the observations to gravity waves with rather long vertical wavelengths $\lambda_z >$ 15 km because of the observational filter of AIRS (e.g., Alexander 1998; Wu et al. 2006).

The Temperature Lidar for Middle Atmosphere Research (TELMA), recently developed at DLR and first deployed at Lauder during DEEPWAVE, is a transportable, semiautonomous middle atmosphere lidar (Kaifler et al. 2015). From the measured photon count profiles temperature profiles are determined by top-down integration assuming hydrostatic equilibrium (Hauchecorne and Chanin 1980). At the top altitude of around 100–110 km, the integration is initialized by the nearest available SABER temperature measurements. Here, hourly mean profiles between 30 and 85 km are used to document the stratospheric and mesospheric temperature evolution over the SI and to compare the observations with the IFS output interpolated to the position of Lauder.

3. Tropospheric circulation for June–August 2014

In this section, we first analyze the Southern Hemispheric tropospheric circulation situation during austral winter 2014 and highlight its impact on the tropospheric circulation in the vicinity of New Zealand. Then, we compare the daily tropospheric circulation patterns of New Zealand to their long-term occurrence properties and relate them to wave forcing and to reported wave activity during the DEEPWAVE period.

a. Circulation patterns

Typical patterns of the Southern Hemispheric tropospheric circulation are analyzed with the help of three commonly used climatological indices. The Southern Oscillation index (SOI) is the difference in mean sea level pressure (MSLP) between the western and eastern tropical Pacific. In the austral winter months of June–August (JJA), negative SOI values are associated with anomalous southwesterly flow over New Zealand (Gordon 1986) and a higher mean seasonal frequency of blockings (Kidson 2000). In 2014, the monthly mean SOI taken from NCEP–NCAR

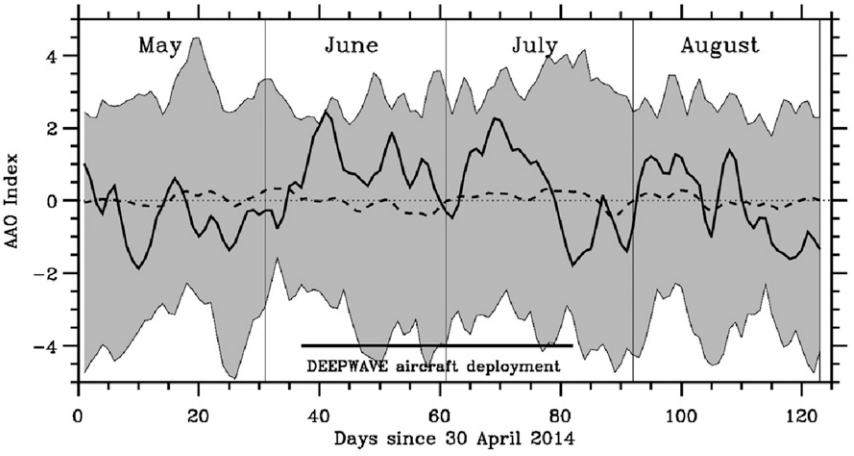

FIG. 1. Daily SAM/AAO index for May–August 2014 (solid line). The gray-shaded area encloses the minima and maxima from 36 years' worth of NCEP–NCAR reanalysis data and the dashed line shows the climatological mean.

reanalyses (http://www.cpc.ncep.noaa.gov/data/indices/soi) switched from positive values in April–June (0.8, 0.5, and 0.2) to negative values in July–September (−0.2, −0.7, and −0.7), indicating an increasing tendency for southwesterly flows and blocking over New Zealand.

The index of the southern annular mode (SAM) or Antarctic Oscillation (AAO) is calculated as the difference of the normalized zonal MSLP between 40° and 60°S (Gong and Wang 1999). During JJA, the STJ and PFJ are two bands of strong westerlies that, climatologically, are located north and south of New Zealand at around 30° and 50°S, respectively (Gallego et al. 2005). The STJ is the dominant jet reaching its maximum magnitude between June and mid-September. The position, strength, and occurrence frequency of both jets depend differently on the sign of the SAM index. During positive SAM phases, the STJ is weaker. During austral winter, positive SAM phases are correlated with enhanced PFJ occurrence and peak wind speeds. Analyzing the daily evolution of the SAM index of the NCEP–NCAR reanalysis reveals that the aircraft deployment of DEEPWAVE took place during a period with moderately positive SAM anomalies (Fig. 1). This implies slightly stronger-than-average PFJ westerlies at mid- to high latitudes (50°–70°S) and slightly weaker-than-average STJ westerlies in the midlatitudes (30°–50°S).

The semiannual oscillation (SAO) of the Antarctic troposphere results from the twice-yearly expansion and contraction of the circumpolar pressure trough. In a year with a pronounced SAO, the circumpolar pressure trough is deepest and located farther south in the equinoctial seasons of March–May and September–November. In winter and summer, the trough expands equatorward and becomes less intense (Burnett and McNicoll 2000). To quantify an SAO index in the region of New Zealand, the monthly mean daily MSLP difference between 44° and 70°S at 172°E was determined using ERA-Interim data. The resulting index revealed a generally weak local SAO for the year 2014 (not shown). This indicates a contraction of the tropospheric westerlies in the midlatitudes and an enhancement of blocking in the vicinity of New Zealand during DEEPWAVE (Burnett and McNicoll 2000; Trenberth 1986).

b. *Synoptic flow regimes*

Some years ago, Kidson (2000) introduced 12 characteristic synoptic flow regimes over New Zealand as daily weather types. His classification is based on surface circulation patterns derived from a cluster analysis using the 40-yr (1958–97) NCEP–NCAR reanalysis dataset. Kidson's weather types were often used in climate variability studies (e.g., Renwick 2011 and references therein). Here, we investigate the occurrence frequency of these patterns during JJA 2014 and relate them to the tropospheric forcing conditions and mountain wave activity during DEEPWAVE. The analysis is based on the archive of the National Institute of Water and Atmospheric Research (NIWA) of New Zealand, which provides an objective classification of 0000 and 1200 UTC NCEP–NCAR reanalyses as described in Renwick (2011) that also includes recent years. In the next paragraph, we first present the occurrence frequency of weather types together with selected charts of the according ECMWF IFS 1000-hPa geopotential height and horizontal wind at 850 hPa. The occurrence frequencies are then compared to the results of the long-term studies of Kidson (2000) and Renwick (2011). Second, we present the patterns that occurred during

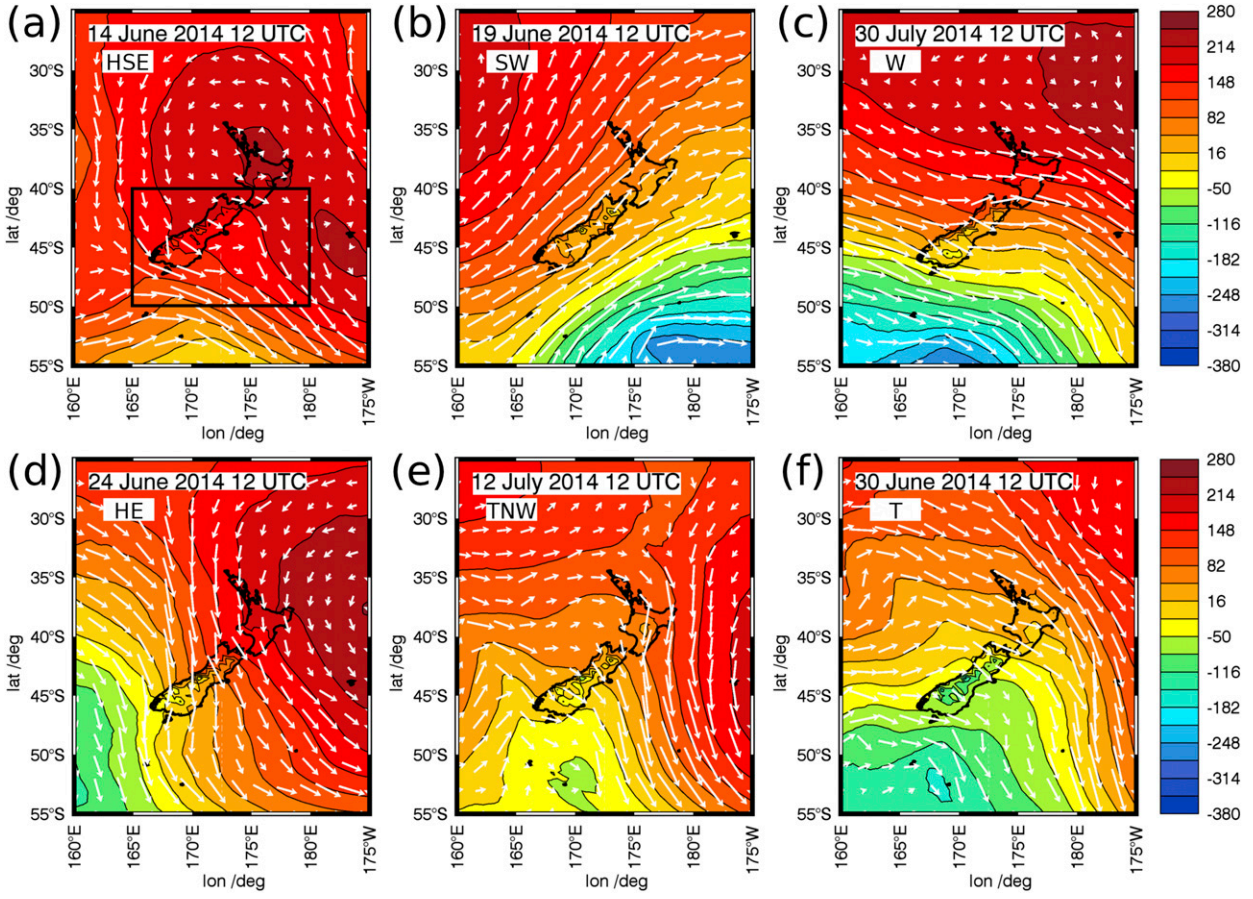

FIG. 2. Selected examples of the ECMWF IFS 1000-hPa geopotential height (m) and horizontal wind at 850 hPa (white arrows) for weather regimes occurring during JJA 2014: (a) HSE (IOP 3, RF04), (b) SW (IOP 6, RF07), (c) W (GB21), (d) HE (IOP 8, RF09), (e) TNW (IOP 13, FF09), and (f) T (IOP 9, RF13, FF01, FF02). Box in (a) marks the area used for spatial mean profiles presented in Figs. 3–5.

IOPs with mountain waves as the primary target, and we relate them to the reported wave activity.

The most common circulation pattern during JJA 2014 was a high pressure system centered at the southeast coast (HSE, Fig. 2a) of the SI (21.7% of 184 reanalyses at 0000 and 1200 UTC). The HSE regime causes weak pressure gradients and, therefore, weak surface winds in the vicinity of the SI. The second most-common pattern was the southwest (SW) regime, with an occurrence frequency of 17.9%. This regime is characterized by a high pressure system to the northwest and a trough east of New Zealand, resulting in a southwesterly flow incident on the SI (Fig. 2b). Other common patterns were a high pressure system located over New Zealand, with the strongest gradient and wind toward the south (H regime; not shown) with an occurrence frequency of 15.2%, and a high pressure system north of the North Island, with a strong pressure gradient toward the south leading to a strong westerly flow (W regime; Fig. 2c). The latter flow regime is prone to excite mountain waves and was found for 9.8% of the reanalyses. It prevailed for some consecutive days only at the end of July and beginning of August, after the aircraft deployment concluded [ground-based lidar and radiosonde observations continued through this period at Lauder; see Kaifler et al. (2015) and Ehard et al. (2017)]. Similar to the SW regime, a high pressure system close to the North Island's west side caused a moderate southwesterly flow on the SI (HNW, not shown; 7.6%). A high pressure system east (HE) of the North Island (5.4% or 5 days) is associated with relatively strong northwesterly winds nearly perpendicular to the main ridge of the Southern Alps (Fig. 2d). Situations with a trough located west of New Zealand (TNW regime; Fig. 2e) causing northwesterly winds or the trough axis (T) directly above New Zealand, resulting in a moderate westerly flow (Fig. 2f), occurred for 4.9% and 4.3% of the reanalyses, respectively. The

TABLE 1. Weather regimes of DEEPWAVE IOPs focusing on mountain and trailing waves around the SI based on the available objective classification of NIWA using NCEP–NCAR reanalysis data at 0000 and 1200 UTC. Compare also with Table 4 in Fritts et al. (2016) for summaries of the research flights of the NSF/NCAR GV (RF) and the DLR Falcon (FF).

					Weather regime	
IOP	RF	FF	Date	Target	0000 UTC	1200 UTC
1	1		6 Jun	MW/TW/PF SI	HSE	HSE
3	4		14 Jun	MWs/TWs SI	HSE	HSE
4	5		16 Jun	MWs/TWs SI	HE	TNW
6	7		19 Jun	MWs/CWs/FWs E. Ocean	SW	SW
7	8		20 Jun	MWs/TWs SI	SW	W
8	9		24 Jun	MWs SI	HE	HE
	10		25 Jun	MWs/TWs SI	TNW	W
9	12	1/2	29 Jun	MWs/TWs SI	TNW	TNW
	13		30 Jun	MWs SI	TNW	T
	14		1 Jul	MWs/TWs SI	T	T
10	16	4/5	4 Jul	MWs/TWs SI	SW	SW
13	20	6	10 Jul	PF/MW SO SI	HE	HE
	21	7/8	11 Jul	MWs SI	HE	HE
	22	9	12 Jul	MWs SI	TNW	TNW
		10	13 Jul	MWs SI	TNW	TSW
15		12	16 Jul	MWs SI	HSE	HSE
16	26		20 Jul	MWs SI along mountain ridge	TSW	TSW

other regimes occurred for less than 4% of the reanalyses. They comprise a trough reaching the east coast toward the northern part of New Zealand, resulting in a weak southerly to southeasterly flow over the SI (TSW regime), a low located northwest and a high located southeast of New Zealand causing a weak northeasterly flow (NE regime), a high pressure system west of the SI (HW), and a ridge bridge over the SI (R regime) characterized by weak pressure gradients and, therefore, weak surface winds in the vicinity of the SI (not shown). Comparing those findings to the values found by Renwick (2011) for JJA of 1958–2010, the occurrence frequency was twice as high for the HSE regime in 2014 (21.7% vs 10.6%), enhanced for the SW regime (17.9% vs 11.3%) and strongly reduced for the T regime (4.3% vs 15.8%). The mean duration of the different regimes was found to be 1–2 days in the 40-yr NCEP–NCAR reanalysis dataset (Kidson 2000). For JJA 2014, we found them to last mainly 1–4 days. The HSE blocking pattern persisted even longer in the first half of June. As already mentioned the W regime prevailed for some consecutive days only at the end of July and beginning of August.

Kidson (2000) grouped the 12 flow regimes into three classes, representing the zonal group (H, HNW, and W), the trough group (T, SW, TNW, and TSW), and a blocking group (HSE, HE, NE, HW, and R). During the winter months of his 40-yr dataset Kidson calculated the relative portions to be 28%, 40%, and 32%, respectively. Renwick's (2011) results extending the analysis till 2010 only differ slightly (29%, 39%, and 31%). For JJA 2014, the relative group fractions are 33%, 31%, and 36%, respectively. These numbers show that the trough group was underrepresented in JJA 2014 whereby the SW regime was the most common of all trough group members. Altogether, the blocking regimes dominated during DEEPWAVE. The latter finding is especially true when the time period of the aircraft deployment (6 June–20 July) is considered. During this period, the blocking group dominated even more (49%) and the zonal group was underrepresented (11%). Those findings agree with the indications of the climatological indices presented earlier (SOI and SAO): a tendency for southwesterly flow and blocking over New Zealand.

Table 1 lists the prevailing weather regimes of the IOPs when aircraft measurements sampling mountain waves were conducted in the region of the SI. Although the TNW regime was not one of the most common regimes, it occurred in 4 out of 11 IOPs (Table 1), namely during IOPs 4, 8, 9, and 13 (Fig. 2e). More precisely, the TNW regime occurred on 7 days (at 0000 and/or 1200 UTC) in total and a research flight sampling mountain waves was conducted on five of them. In the majority of those cases, significant and strong mountain wave activity was experienced at flight levels (~13 km for the NSF/NCAR GV and ~10 km for the DLR Falcon; Fritts et al. 2016). Although the SW regime was the second-most frequent, only three IOPs with mountain waves as primary targets were conducted during this regime. It was the relatively weak cross-mountain wind component at 700 hPa that excluded farther SW events as potential cases for aircraft deployments. Therefore, it is worth pointing out that moderate and even strong mountain waves were observed at flight level and also in the mesosphere and lower thermosphere (MLT) for IOP 6 (19 June; Fig. 2b) and IOP 10 (4 July; Smith et al. 2016) in the SW regime. For the HE regime strong mountain waves and wave breaking were observed at flight level and by remote sensing instruments during RF09 in IOP 8 (Fig. 2d; Fritts et al. 2016; Smith et al. 2016). A prominent trough approached New Zealand from the west during IOP 13, resulting in the TNW regime (Fig. 2e) and a northerly-to-northwesterly flow, with moderate-amplitude mountain waves being observed at flight level and a large-scale mountain wave was observed in the MLT on the last day of IOP 13 (Bossert et al. 2015). At this time the regime had already changed from TNW to TSW. For IOPs 1, 3, and 15, which were

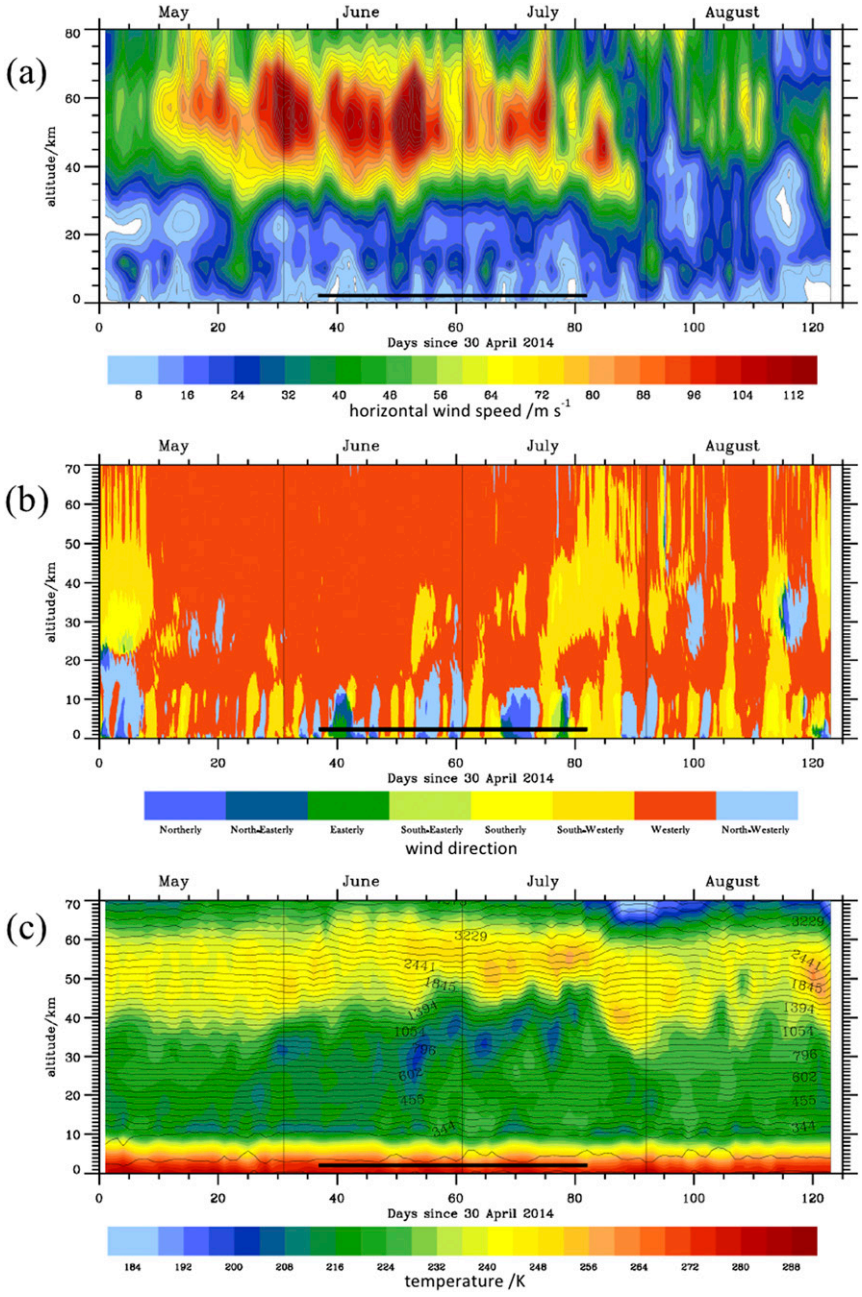

FIG. 3. Vertical profiles of ECMWF $T_L1279/L137$ operational analyses averaged over the area between 40°–50°S and 165°E–180°. (a) Horizontal wind speed ($m\,s^{-1}$, color shaded), (b) wind direction (binned in 45° segments centered around the given wind directions), and (c) temperature (K, color shaded) and potential temperature (K, solid lines). The black solid horizontal lines in each panel mark the DEEPWAVE aircraft deployment period.

classified as HSE regimes (i.e., weak pressure gradients and surface winds), mainly weak mountain wave activity was reported at flight level and in the MLT. A complete summary of the reported gravity wave activity during various IOPs can be found in Fritts et al. (2016).

c. *Vertical profiles over the SI*

Figure 3 shows the temporal evolution of vertical profiles of the horizontal wind, wind direction, and absolute temperature of the ECMWF IFS averaged over an area encompassing the SI (shown by the box in

Fig. 2a) from May to August 2014. Here, we only focus on the troposphere and lower stratosphere. The middle atmosphere is analyzed in section 5. Considering the tropospheric flow conditions, it becomes clear that the surface weather regimes often lead to a directional shear in the lower troposphere (Fig. 3b). There are only a few instances during the DEEPWAVE campaign when the wind does not turn with altitude and is either westerly or southwesterly throughout the troposphere and stratosphere. The other peculiarity visible in Fig. 3a is the periodically occurring enhanced upper-tropospheric and lower-stratospheric wind speed, which is related to the appearance of jet streams (STJ and PFJ) over New Zealand (discussed in more detail in section 4). The tropopause as delineated by the denser isentropes in Fig. 3c is situated mostly around 10-km altitude. Its characteristics are discussed in the following section.

4. Tropopause layer and jets

In this section we analyze the tropopause region and the impact of static stability and wind conditions on the wave propagation during DEEPWAVE. We first analyze the sharpness of the tropopause and make a first estimate about its role in terms of wave reflection. Then, we present the properties of the tropopause jets (STJ and PFJ) and how they relate to the observed wave activity by altering forcing and propagation conditions.

a. Tropopause inversion layer

The vertical change of wind and static stability at the tropopause modifies the properties of vertically propagating gravity waves following the dispersion relationship (e.g., Eckermann and Vincent 1993; Keller 1994; Grise et al. 2010; Shibuya et al. 2015). The height of the tropopause, its sharpness, and the associated shear varied markedly during DEEPWAVE as a result of the presence or absence of tropopause jets originating either from the subtropics or the polar region under wintertime conditions (e.g., Manney et al. 2014). The height of the thermal tropopause (WMO 1957) varied with migratory weather systems. During JJA 2014, the altitude of the thermal tropopause fluctuated between 8- and 13-km altitude, as revealed by Lauder radiosonde and ECMWF IFS temperature profiles (e.g., Fig. 3c). Moreover, the static stability as given by the squared Brunt–Väisälä frequency:

$$N^2 = g\frac{\partial \ln\theta}{\partial z}, \tag{1}$$

where g is gravitational acceleration, z is height, and θ is potential temperature, is usually maximized right above the thermal tropopause (Birner et al. 2002). The associated tropopause inversion layer (TIL) is a global feature of the upper troposphere–lower stratosphere (UTLS; Birner 2006; Grise et al. 2010; Gettelman et al. 2011). Here, we characterize the evolution of the tropopause layer in JJA 2014 by calculating its sharpness in terms of the TIL strength.

Following Gettelman and Wang (2015), the characteristics of the TIL were examined using vertical N^2 profiles derived from ECMWF IFS 6-hourly operational analyses averaged over an area covering the SI of New Zealand (shown by the box in Fig. 2a), which in large part eliminates the signatures of gravity waves. The TIL strengths at the bottom and top relative to the mean values over JJA 2014 are given by

$$\mathrm{TIL}'_{\mathrm{strength,UT}} = \frac{1}{2}\left(N^2_{\mathrm{MAX}} - N^2_{\mathrm{MIN,UT}}\right) - \underbrace{\left\langle \frac{1}{2}\left(N^2_{\mathrm{MAX}} - N^2_{\mathrm{MIN,UT}}\right)\right\rangle_{\mathrm{JJA}}}_{\mathrm{meanTIL_{strength,UT}}} \tag{2}$$

and

$$\mathrm{TIL}'_{\mathrm{strength,LS}} = \frac{1}{2}\left(N^2_{\mathrm{MAX}} - N^2_{\mathrm{MIN,LS}}\right) - \underbrace{\left\langle \frac{1}{2}\left(N^2_{\mathrm{MAX}} - N^2_{\mathrm{MIN,LS}}\right)\right\rangle_{\mathrm{JJA}}}_{\mathrm{meanTIL_{strength,LS}}}, \tag{3}$$

respectively (Fig. 4a). Thereby, N^2_{MAX} is the maximum of N^2 in the UTLS below 20-km altitude, $N^2_{\mathrm{MIN,UT}}$ is the minimum of N^2 in the upper troposphere below the altitude of N^2_{MAX} but above 5-km altitude, and $N^2_{\mathrm{MIN,LS}}$ is the first local minimum of N^2 in the lower stratosphere above the altitude of N^2_{MAX}, where the vertical gradient of N^2 changes from negative to positive. Positive values of the two quantities calculated by Eqs. (2) and (3) characterize a peak in N^2 in the UTLS, which is exceeding the static stability of the stratosphere. Figure 4b illustrates the different quantities by means of three individual N^2 profiles. The mean $\mathrm{TIL_{strength,UT}}$ averaged over the three winter months of JJA 2014 is $2.6 \times 10^{-4}\,\mathrm{s}^{-2}$ and the mean $\mathrm{TIL_{strength,LS}}$ is equal to $0.96 \times 10^{-4}\,\mathrm{s}^{-2}$. The mean $\mathrm{TIL_{strength,UT}}$ for JJA 2014 is comparable to the values of the annual climatology from 32 yr of ERA-Interim data, as shown in Fig. 7 in Gettelman and Wang (2015), while the mean $\mathrm{TIL_{strength,LS}}$ was larger ($\approx$0.6 vs $0.96 \times 10^{-4}\,\mathrm{s}^{-2}$). This enhancement can probably be explained by the presence of weak gravity waves signals still contained in the spatial mean profiles in the lower stratosphere altering the N^2 values in the lower

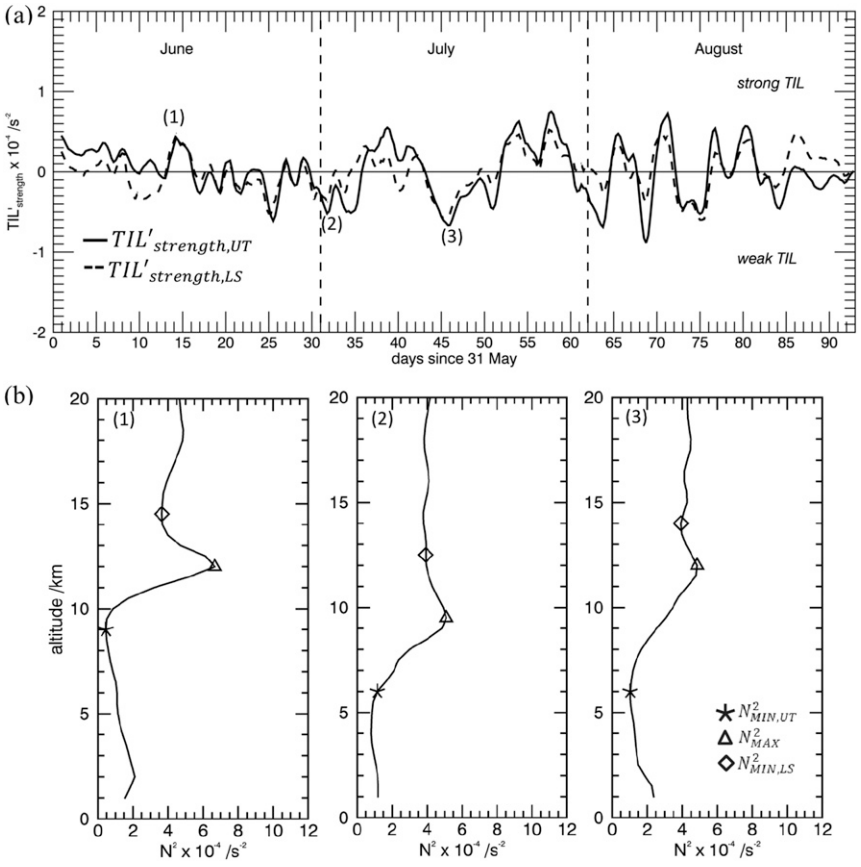

FIG. 4. (a) TIL characteristics $TIL'_{strength,UT}$ (black solid) and $TIL'_{strength,LS}$ (black dashed) as 24-h running mean based on 6-hourly ECMWF analysis. (b) Examples of mean profiles of N^2 from which TIL characteristics were calculated are taken on 1) 14 Jun (IOP3, RF04), 2) 2 Jul (after IOP9, RF14), and 3) 16 Jul 2014 (IOP 15, FF12). Symbols mark $N^2_{MIN,UT}$ (star), N^2_{MAX} (triangle), and $N^2_{MIN,LS}$ (diamond).

stratosphere (see, e.g., the wavy structures between 13- and 20-km altitude in Fig. 4b).

Generally, the TIL is quite pronounced when the two quantities $TIL'_{strength,UT}$ and $TIL'_{strength,LS}$ are positive, which means there is a discernable peak (i.e., large strength) in stability (Fig. 4a, an example profile is shown in the first panel of Fig. 4b). The TIL is weak when $TIL'_{strength,UT}$ and $TIL'_{strength,LS}$ are negative, which means there is no pronounced peak (i.e., small strength) in stability (Fig. 4a; example profiles are shown in the second and third panels in Fig. 4b). Besides the variability of the TIL characteristics, periods of some consecutive days with a strong and well-pronounced TIL are found in Fig. 4a in the middle of June and in the first and second half of July. During those days the SI was influenced by high pressure systems (namely the HSE, HE, and H regimes), that is, anticyclones, which are known to have pronounced TIL characteristics (Wirth 2003, 2004).

b. Hydrostatic reflection coefficient

While the reflection of nonhydrostatic gravity waves at the tropopause is a function of wavenumber and the depth of the tropopause, the hydrostatic reflection coefficient (Eliassen and Palm 1960) can be easily calculated for a large Richardson number (Ri $\gg$ 1/4), that is, no or negligible vertical shear, according to

$$r \approx \frac{N_S - N_T}{N_T + N_S}, \tag{4}$$

where N_T and N_S are the representative mean Brunt–Väisälä frequencies of the troposphere and the stratosphere (Keller 1994). A reflection coefficient of 1 reveals the total reflection of hydrostatic gravity waves. For typical midlatitude conditions, $N_S = 2\text{–}4 \times N_T$, such that the reflection coefficient varies between 0.33 and 0.6, indicating a partial reflection of vertically propagating hydrostatic gravity waves (Gill 1982). We use this as a

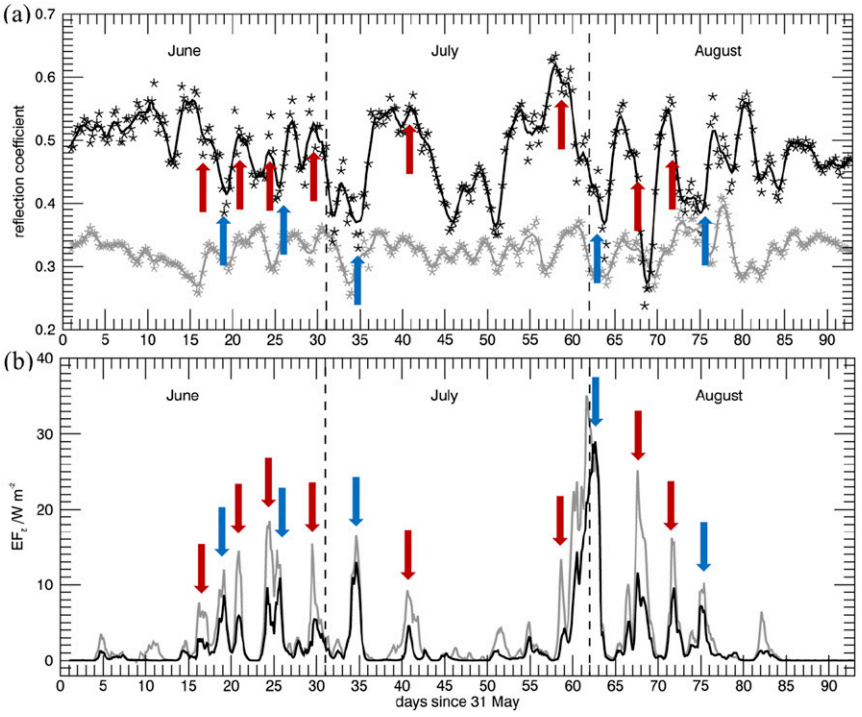

FIG. 5. (a) Hydrostatic reflection coefficients r (valid for Ri $\gg$ 1/4) from ECMWF 6-hourly operational analyses (stars) and 24-h running means (solid lines) using an averaged stratospheric value of N (gray) and N_{MAX} taken in the UTLS (black). (b) The 3-hourly regional vertical energy fluxes over SI computed from WRF constrained by MERRA2 initial conditions at 4- (gray) and 12-km (black) altitude. Arrows mark the GW events, when the reflection coefficient is close to or larger than 0.5 and the EF$_z$ at 12 km is reduced by 47%–77% (red) from the 4-km value and when the reflection coefficient is close to or smaller than 0.4 and the EF$_z$ is reduced by <35% (blue).

first simple approach to investigating the influence of the TIL on wave propagation, being aware that we neglect the influence of the vertical shear, the depth of the TIL, and the influence of the wave's vertical wavelengths. The reflection coefficient was evaluated using two different methods for the period JJA 2014. First, mean values of N_T and N_S were calculated for selected layers in the troposphere (z = 3–6 km) and the stratosphere (z = 16–19 km). Second, instead of using the mean stratospheric value N_S in Eq. (4), N_{MAX} in the UTLS was taken in order to evaluate the influence of the TIL on the magnitude of the reflection coefficient. Figure 5a shows both results computed for JJA 2014. The reflection coefficient varies between 0.25 and 0.41 when the mean tropospheric-to-stratospheric stabilities are considered. The reflection coefficient becomes significantly larger if the enhancement of static stability by the TIL is taken into account. Maximum values often exceed r = 0.5 and values of up to 0.63 were calculated for a short period near the end of July 2014.

We compared the temporal evolution of the reflection coefficient calculated with the N_{MAX} values (black stars in Fig. 5a) with the regional vertical energy fluxes EF$_z$ over SI derived from the long-term WRF simulations (Fig. 5b). Only mountain wave episodes (i.e., 6-hourly values with EF$_z$ $\geq$ 6 W m^{-2} at 40-km altitude) were considered. When the reflection coefficient is close to or larger than 0.5, EF$_z$ values at 12-km altitude were reduced by 47%–77% (20th and 80th percentiles, i.e., for 16 out of 20 points in time the reduction was larger than 47%) compared to the EF$_z$ values at 4-km altitude (red arrows mark those events in Fig. 5). The reduction is below 35% (80th percentile, i.e., for 12 out of 15 points in time the reduction is below 35%) when the reflection coefficient is close to or below 0.4 (blue arrows mark those events in Fig. 5). The simulated reduction in EF$_z$ for a given value of the reflection coefficient is larger than predicted by linear theory, where the net upward flux is $(1 - r^2)$ times the flux of the incident wave (Eliassen and Palm 1960). This means for r = 0.5 that one would expect a reduction of EF$_z$ by 25% rather than 50%. This discrepancy might be explained by the fact that reflection due to vertical shear is not considered in

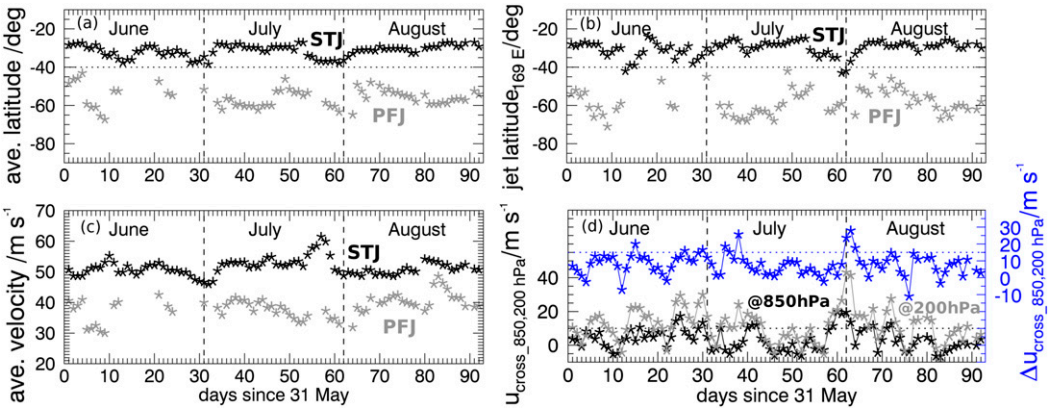

FIG. 6. Zonally averaged (a) latitudes and (c) strengths of the STJ (black stars) and the PFJ (gray stars) during JJA 2014. (b) Latitudes of the STJ and the PFJ at 169°E. Operational IFS analyses at 200 hPa at 0600 UTC were analyzed using the method presented by Gallego et al. (2005). (d) The cross-mountain (NW direction) velocity of operational IFS analyses averaged over NZ at 850 hPa (black) and 200 hPa (gray) and their difference [e.g., vertical shear between 850 and 200 hPa (blue)].

the approximated r given by Eq. (4) and vertical shear certainly played a role during the gravity wave events (Fig. 3). Nevertheless, the Pearson correlation coefficient between the reflection coefficient based on N_{MAX} and the EF_z reduction (between 4 and 12 km) is 0.70 when the 6-hourly values of the events marked by arrows in Fig. 5 are considered. Therefore, the relationship between the reflection coefficient and the EF_z reduction in the lower stratosphere highlights the impact of the TIL on the vertical propagation of mountain waves. A stronger TIL enhances the reflection of hydrostatic MWs and, thus, reduces the vertical energy flux.

c. *Subtropical and polar front jets*

In addition, the tropopause jets (STJ and PFJ) were analyzed based on the method followed by Gallego et al. (2005), where the jets are determined by searching for closed circumpolar 200-hPa geostrophic streamlines showing the largest mean horizontal wind speed along the streamline. Here, operational ECMWF IFS analyses of geopotential heights and horizontal winds at 200 hPa were used. From the results, the zonally averaged positions and strengths of the STJ and the PFJ were determined for the 0600 UTC analyses (Figs. 6a,c). The STJ dominated the circulation with a mean wind speed of 51 m s^{-1} and its mean location being at 31°S. The PFJ was present on only half of the days in June but was more frequent in July and August (more than 80% of the days). Its mean wind speed was 39 m s^{-1}, which is more than 10 m s^{-1} slower than the STJ, and the mean location was at 56°S. This matches the climatological findings presented by Gallego et al. (2005). Although the connection mentioned above between the SAM index and the strength of STJ and PFJ (section 3) does not hold for daily values, it matches for temporally averaged values. While the daily SAM index was mainly positive in June and the first half of July (Fig. 1), the mean strengths of the STJ and the PFJ were 51 and 38 m s^{-1}, respectively. For the second half of July, when the daily SAM index was mainly negative, the mean strengths of the STJ and the PFJ were 55 and 36 m s^{-1}, respectively. The difference in wind speed is small but the SAM index was not as positive or negative as for other years represented by the gray area in Fig. 1.

Since the focus of this paper is on the SI of New Zealand, the location of the jets was also analyzed at 169°E (Fig. 6b). At that longitude, the STJ was located south of 35°S on 13–15 June (IOP 3), 24 June (IOP 8), 28–29 June (IOP 9), and 31 July–2 August (GB 21). On 13 June and 31 July–1 August the location was even south of 40°S. The PFJ was located north of 52°S at 169°E in the beginning of June, on 21 June (GB 10), 1 July (IOP 9), 19–20 July (IOP 16), 24 July, and on some days in August (e.g., 4, 7, 9, and 11–13). On 1 and 19 July and 7 and 11 August the PFJ was located even north of 47°S. The locations of the PFJ and STJ were compared with the gravity wave activity reported in the flights summaries of the DEEPWAVE IOPs (Table 4 in Fritts et al. 2016). Whenever the STJ was located close to the SI, mountain waves and sometimes even jet-stream-induced gravity waves were observed at flight level, in the stratosphere, and the MLT. Additionally, wave breaking and turbulence at flight level were reported for these events. For the cases where the PFJ was located close to the SI, weak mountain wave activity at flight level was reported. Yet, surprisingly strong mountain wave activity in the stratosphere and the MLT were also

reported. This suggests that the presence of the STJ was associated with stronger forcing conditions and larger positive (negative) vertical shear below (above) the jet maximum. These conditions not only triggered strong mountain waves but also affected the wave propagation and led to wave breaking in the UTLS. The presence of the PFJ was linked with weaker forcing but the triggered mountain waves could propagate farther up, leading to strong mountain wave signals in the MLT. The difference in the forcing conditions and in the vertical shear between the STJ and the PFJ is largely confirmed by the cross-mountain winds (northwesterly direction) at 850 and 200 hPa from IFS analyses averaged over the New Zealand (NZ) area as shown in Fig. 6d. When the STJ was close to the SI (e.g., 14 June, 24 June, 29 June, and 31 July–1 August), cross-mountain winds at 850 hPa were often larger than $10\,\mathrm{m\,s^{-1}}$ and at 200 hPa larger than $20\,\mathrm{m\,s^{-1}}$, leading to a larger vertical shear (i.e., differences of around $15\,\mathrm{m\,s^{-1}}$ and more between 850 and 200 hPa; blue curve in Fig. 6d). This was different when the PFJ was close to the SI (e.g., 1–4 June and 19–24 July), where the cross-mountain winds at 850 and 200 hPa hardly reach $10\,\mathrm{m\,s^{-1}}$ because the PFJ is generally weaker than the STJ and approaches New Zealand from its mean location from the south (see previous paragraph). The Pearson correlation coefficients between the latitude of the STJ and the cross-mountain winds at 850 and 200 hPa are -0.46 and -0.47, respectively. The negative sign comes from the negative latitudes used for the Southern Hemisphere. Those analyses support the findings of Kaifler et al. (2015) and the hypothesis that the PFJ is the main driver when weak and moderate mountain wave activity were observed in the UTLS and large amplitudes in the MLT.

5. Stratospheric and mesospheric wind and thermal conditions

The wind minimum in the lower and middle stratosphere is a well-known climatological feature in midlatitudes and became the focus of recent research as it largely controls the deep vertical propagation of gravity waves into the upper stratosphere and mesosphere (Kruse et al. 2016). In this section we first analyze the stratospheric circulation during DEEPWAVE influenced by planetary waves. NAVGEM reanalyses then allow us to extend the picture of the prevailing wind and thermal conditions up to 110-km altitude.

a. Stratospheric circulation

To characterize the stratospheric conditions during the DEEPWAVE campaign, Fig. 7 shows the zonally averaged absolute temperature T and the horizontal wind speed V_H for JJA 2014 together with the T and V_H anomalies with respect to the climatological means as derived from ERA-Interim data. During the course of the three winter months, the cold region inside the polar vortex and the stratopause above gradually subsided. Associated with this shift is a change in the inclination of the polar vortex, as seen by the axis of the strongest wind V_H in the PNJ. Especially in June and July 2014, New Zealand (35°–45°S) was located below a zone of pronounced meridional and vertical shear of the stratospheric wind. Equatorward, the STJ extended from 25° to about 40°S and dominated the flow in the lower stratosphere. Figures 7b, 7d, and 7f depict the wind and temperature anomalies. Especially over the New Zealand region, the upper-stratospheric winds in July and August are up to $10\,\mathrm{m\,s^{-1}}$ weaker than the climatological averages. This decline is associated with a poleward shift of the stratospheric wind maximum, indicating a displacement of the polar vortex away from New Zealand.

The anomalies of geopotential height Z and horizontal wind V_H at the 30-hPa pressure surface, as well as the modified potential vorticity $\mathrm{MPV} = \mathrm{PV} \times (\Theta/475\,\mathrm{K})^{4.5}$ (Lait 1994) at the 600-K isentropic surface (approximately 25-km altitude) from the 36-yr climatological average of ERA-Interim, illustrate the displacement and deformation of the shape of the polar vortex in the austral winter 2014 (Fig. 8). The poleward displacement of the polar vortex in the southern Pacific sector containing New Zealand is represented by positive height and MPV anomalies (i.e., MPV was less negative) in JJA 2014. There is a weak quadrupole structure in Z and V_H over the South Pole region, indicating a weak influence of planetary wavenumber-2 (PW2) activities. The stratospheric horizontal wind was weaker in a latitude belt extending from 35° to 50°S while it was much stronger than the climatological average farther south (Fig. 8, right column).

Figure 9 shows the zonal mean temperatures from MLS (T_{MLS}) and ERA-Interim ($T_{\mathrm{ERA\text{-}I}}$) and the zonal wind from ERA-Interim ($U_{\mathrm{ERA\text{-}I}}$) for the winter months JJA 2014. To set the results for the year 2014 (plotted with red lines) into the climatological context of the previous years, 12 years of MLS and 36 years of ERA-Interim profiles are plotted as gray lines. Higher-than-average lower-/middle-stratospheric temperatures and lower-than-average upper-stratospheric temperatures are found for JJA 2014. Especially in July 2014, the temperature was 2–4 K higher than in the mean value and for $T_{\mathrm{ERA\text{-}I}}$ even beyond the standard deviation in the stratosphere from 15- to 30-km altitude. In the upper stratosphere up to the height of the stratopause, $T_{\mathrm{ERA\text{-}I}}$

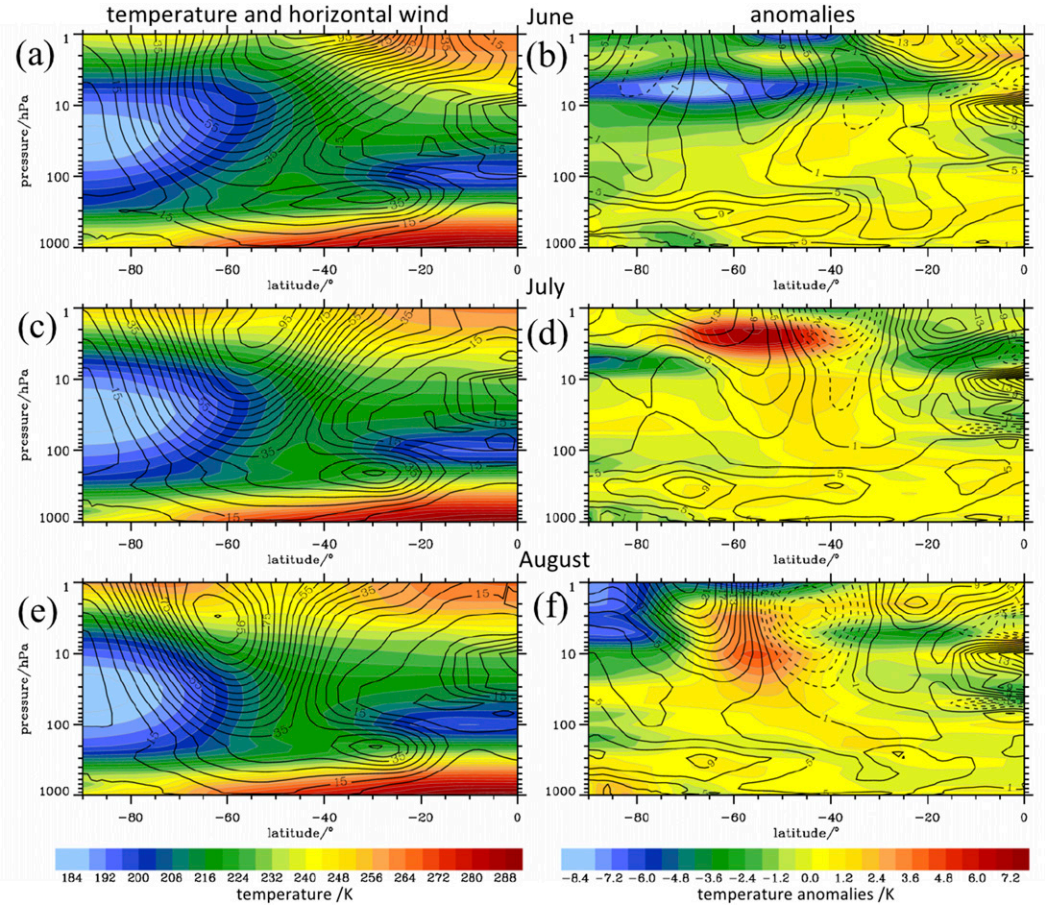

FIG. 7. (left) Monthly mean zonally averaged absolute temperature (K, color shaded) and horizontal wind ($m\,s^{-1}$, solid lines) for (a) June, (c) July, and (e) August 2014. Data shown are 6-hourly ECMWF $T_L1279/L137$ operational analyses on 25 pressure levels interpolated onto a regular $1° \times 1°$ latitude–longitude grid. (right) Temperature (K, color shaded) and horizontal wind ($m\,s^{-1}$, with solid lines for positive and dashed lines for negative values) anomalies of the operational analyses for (b) June, (d) July, and (f) August 2014 from the 36 years' worth of ERA-Interim climatological mean data (6-hourly monthly mean of daily mean data interpolated onto the same latitude–longitude grid).

was up to 10 K lower than the climatological mean, which led to a reduced temperature gradient below the stratopause. In the ERA-Interim data, there is a clear trend of the seasonal warming in the stratosphere from June to August that is less pronounced in the MLS data. The differences in the vertical profiles might occur as a result of the much lower temporal and horizontal resolution of MLS compared to ERA-Interim. Small-scale effects like GWs are likely not well represented in the MLS measurements since the temporal resolution is 1 day at one place. The zonal wind profiles show the characteristic properties with a tropopause jet of $U_{MAX} \approx 30\,m\,s^{-1}$ at 10–12-km altitude, a stratospheric wind minimum between 20- and 30-km altitude, and a pronounced increase in $U_{ERA\text{-}I}$ of about $3\,m\,s^{-1}\,km^{-1}$ into the PNJ. Whereas the mean profile for June 2014 was close to the climatological mean (and situated inside the limits given by the standard deviations), the July and August profiles deviate significantly from the climatology with less-than-average stratospheric winds.

b. *Planetary waves*

Figure 10 shows the vertical profiles of the amplitudes of stationary planetary waves with zonal wavenumbers 1 and 2 (PW1 and PW2) averaged for the latitude band of New Zealand for the months JJA derived from MLS geopotential height data. As such, the amplitudes do not represent a conservative measure of wave activity. Wave activity strictly related to the Eliassen–Palm (EP) flux and its divergence is given further below. Again, to set the climatological context, profiles from all 12 MLS years are added to the plots. The PW1 amplitude was

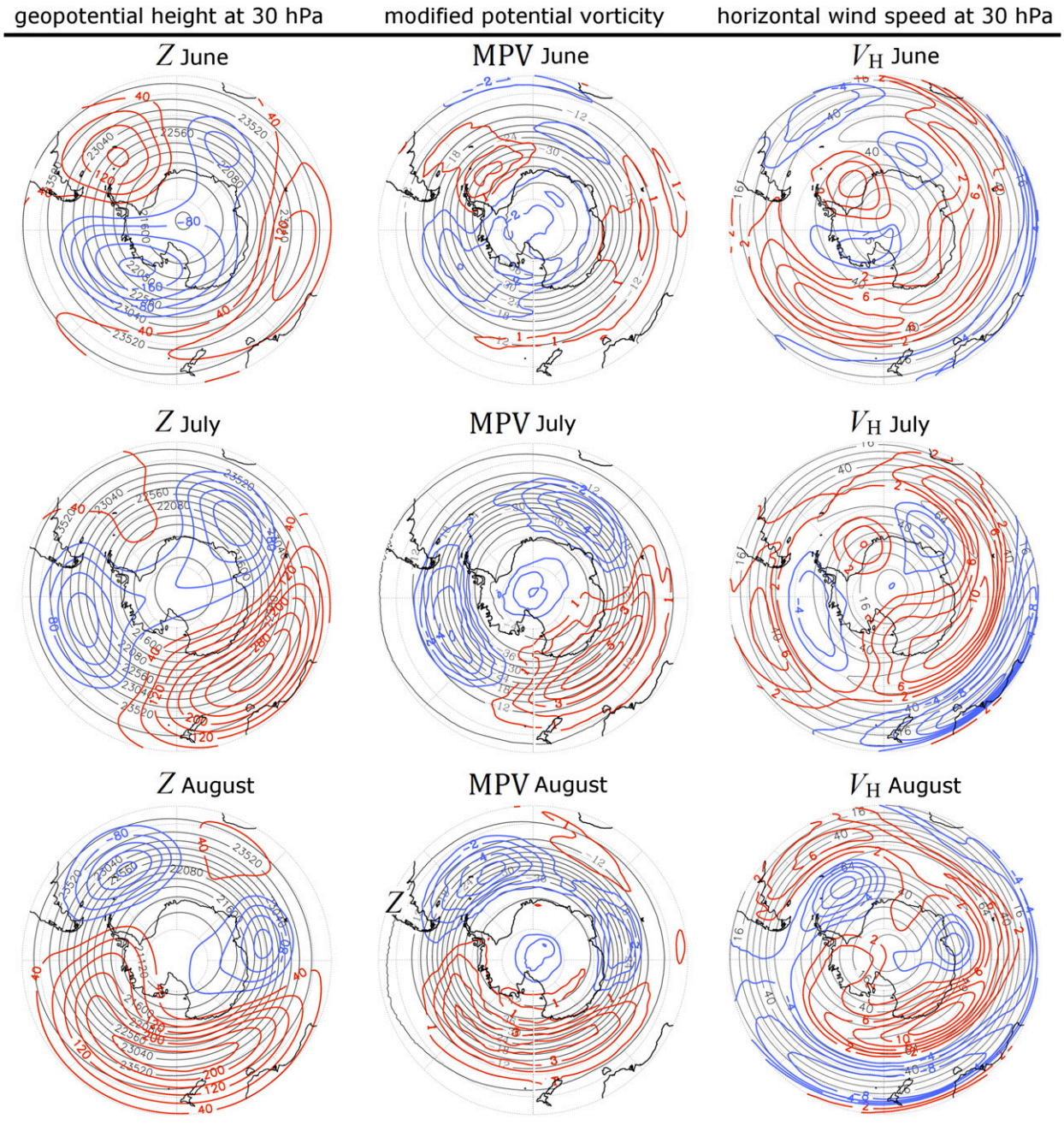

FIG. 8. (left) Positive (negative) anomalies shown as red (blue) contours of geopotential height Z at 30 hPa (m), (middle) modified potential vorticity (MPV) at 600 K (PVU, where 1 PVU = 10^{-6} K kg^{-1} m s^{-1}), and (right) horizontal wind speed V_H at 30 hPa (m s^{-1}) for (top) June, (middle) July, and (bottom) August 2014 from 36-yr climatological average of ERA-Interim monthly means (gray solid contours).

weak in June 2014 in the middle and upper stratosphere and partly even below the standard deviation. In July and August 2014, the PW1 amplitude was much stronger than the climatological mean (black curves in Fig. 10) and exceeds even the standard deviation in August. The PW2 amplitude in winter 2014 is weaker than the climatological mean except in the mesosphere in June and between 20 and 35 km in August 2014. These time and altitude ranges are the only ones where the magnitudes of the PW1 and PW2 amplitudes are similar. Generally, the amplitude of the PW2 is weaker than that of the PW1. PW analysis using the ERA-Interim data

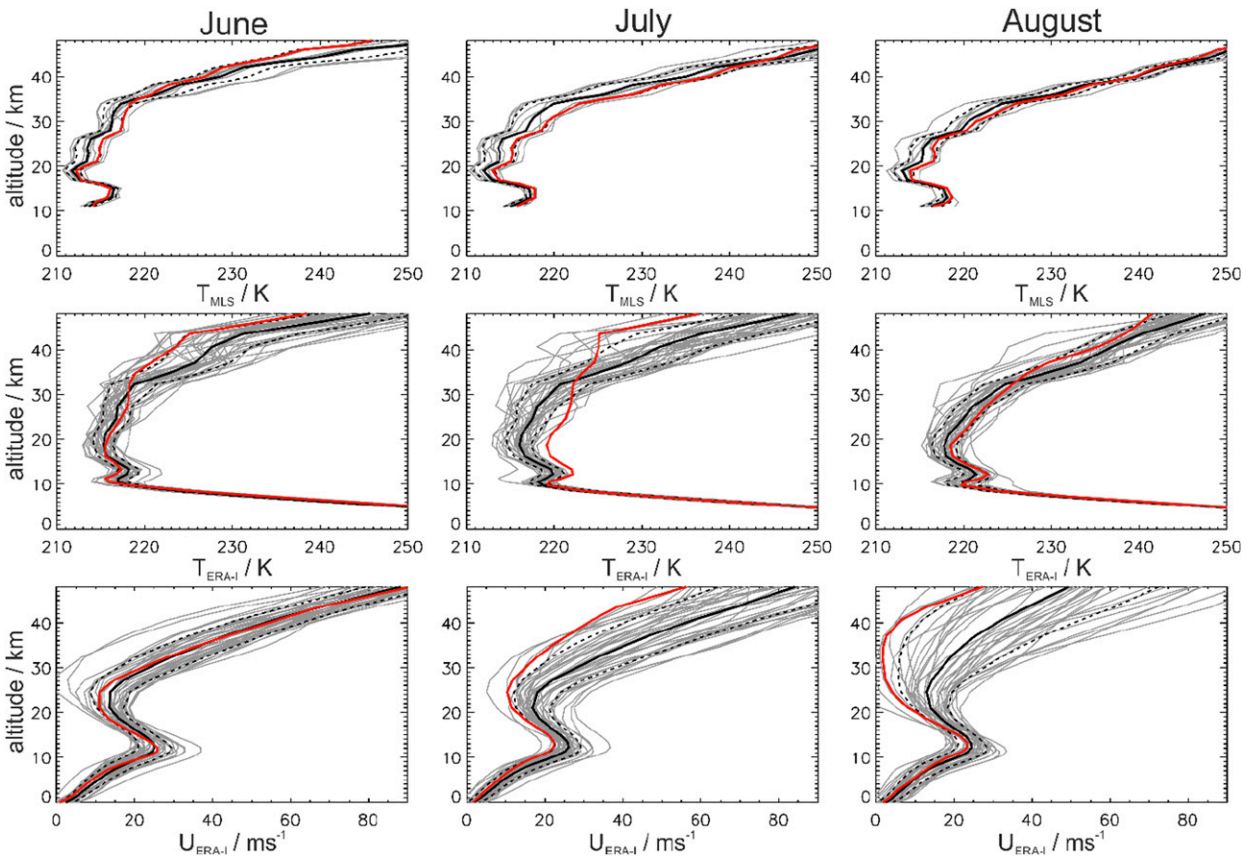

FIG. 9. Vertical profiles of the monthly mean and zonal-mean (top) MLS temperatures (T_{MLS}), (middle) ERA-Interim temperatures ($T_{ERA\text{-}I}$), and (bottom) ERA-Interim zonal winds averaged around NZ (35°–45°S, 160°E–180°). Thin gray lines represent the means from all available years (MLS = 12, ERA-Interim = 37). Solid black lines are the long-term averages and their respective standard deviations are plotted by dashed lines. The red lines represent the means for the DEEPWAVE year 2014.

largely agrees with the presented results of MLS with respect to the amplitudes of PW1 and PW2 (cf. Fig. C1 of appendix C).

Figure 11 illustrates the temporal evolution of the PW1 and PW2 amplitude of MLS by means of altitude–time plots averaged between 35° and 45°S and by latitude–time plots averaged between 30 and 40 km. At New Zealand's latitudes, the PW1 amplitude is maximized at 30–70 km in mid-/late July and at 40–65 km in mid-/late August. The strongest PW1 amplitudes occurred between 50° and 70°S during mid-July and the end of August. The PW1 amplitudes increased significantly at the end of June between 45° and 65°S and were maximized at around 18 July 2014. Afterward, the amplitude varied regularly but stayed large. PW2 amplitudes were maximized nearly every 21 days, centered on 23 June, 18 July, 7 August, and 27 August 2014 (Figs. 11c,d) and were most pronounced below 50 km around New Zealand's latitudes. The strongest PW2 amplitudes occurred between 50° and 70°S during mid- to late August.

Thus, the amplitudes given above indicate that the stratosphere above and south of New Zealand was markedly disturbed by PW1 and PW2, displacing the center of the polar vortex during the second half of the DEEPWAVE period. From Fig. 8, it is evident that the polar vortex was shifted away from New Zealand toward South America. As a consequence, the zonal winds in the stratosphere were weaker than average, especially in July and August 2014. In July 2014 the stratospheric wind minimum was anomalously weak compared to the climatological mean.

Figure 12 (left) shows the EP-flux vectors **F** and its divergence $\nabla \cdot \mathbf{F}$ computed as described by Andrews et al. (1987) for the ERA-Interim data of JJA 2014. Altitudes in the troposphere below 5 km are excluded because of artifacts caused by Antarctica. To increase visibility in the stratosphere, which is the main region of interest, the vectors are scaled by $(p_0/p)^{1/2}$ with $p_0 = 1000$ hPa, as in Taguchi and Hartmann (2006). In general, the EP-flux vectors show an upward and

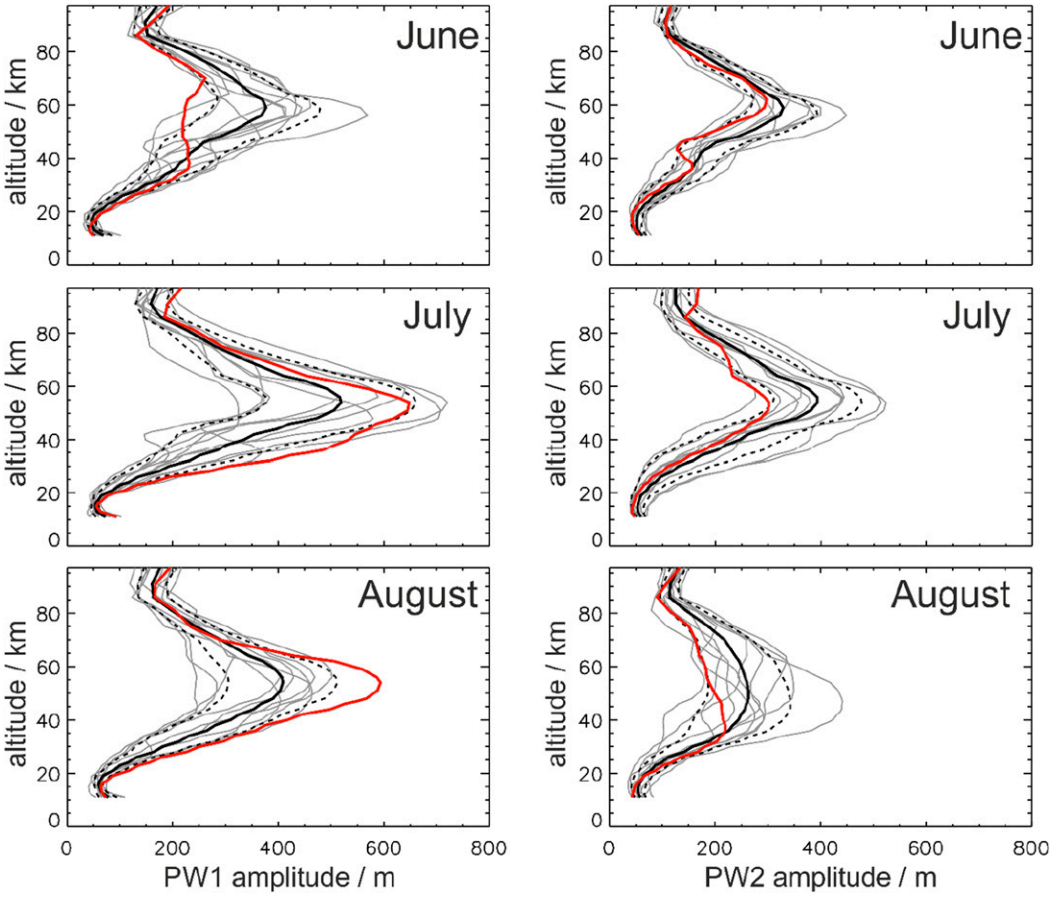

FIG. 10. Vertical profiles of the monthly means of stationary PW1 and PW2 geopotential height amplitudes averaged between 35° and 45°S from MLS for JJA. Thin gray lines represent the means from the 12 available years. Solid black lines are the long-term averages and their respective standard deviations are plotted by dashed lines. The red lines represent the monthly means for the DEEPWAVE year 2014.

equatorward propagation of wave activity south of 30°S in the lower stratosphere. The magnitude of the EP-flux vectors increases and the direction becomes more and more equatorward with increasing altitude. This is valid for all three winter months but the largest magnitudes are found in July and August 2014. This means that the wave activity was greater in July and August compared to June, as already indicated by the PW1 and PW2 amplitudes given above. In July and August, $\nabla \cdot \mathbf{F}$ is convergent (negative values) above 30 km between approximately 20° and 60°S and divergent (positive values) around 35 km between 65° and 75°S. The strongest convergence occurs in the midlatitudes in July 2014. Comparison of $\nabla \cdot \mathbf{F}$ of 2014 with the climatological mean (see Fig. 12, right) shows a much stronger convergence in July and August 2014 in the upper stratosphere than in the climatological mean. The convergence of $\nabla \cdot \mathbf{F}$ is as expected for dissipating and breaking planetary waves originating from the troposphere. It drives an equator-to-pole residual circulation pattern that produces upwelling in the tropics and downwelling in high latitudes (e.g., Dunkerton et al. 1981; Shaw and Perlwitz 2014). This downwelling warms the lower stratosphere and hence changes the meridional temperature gradient, which is related to the vertical zonal wind gradient via the thermal wind balance. Thus, the stratospheric zonal wind is decreased. Both effects, the stratospheric warming and the zonal wind weakening, are shown in Fig. 9.

The enhancement of the magnitude of the EP-flux vectors and of the convergence in the upper stratosphere is in agreement with the overall enhanced planetary wave amplitude found at 40°S (Figs. 10c,e) and the shift of the polar vortex toward South America (Fig. 8). Based on those analyses, we expect that a stronger than normal (i.e., 37-yr mean) poleward refraction of GWs in the upper stratosphere occurred during July and August 2014 (e.g., Ehard et al. 2017) as a result of the enhanced equator-to-pole residual circulation induced by the stronger convergence by PWs.

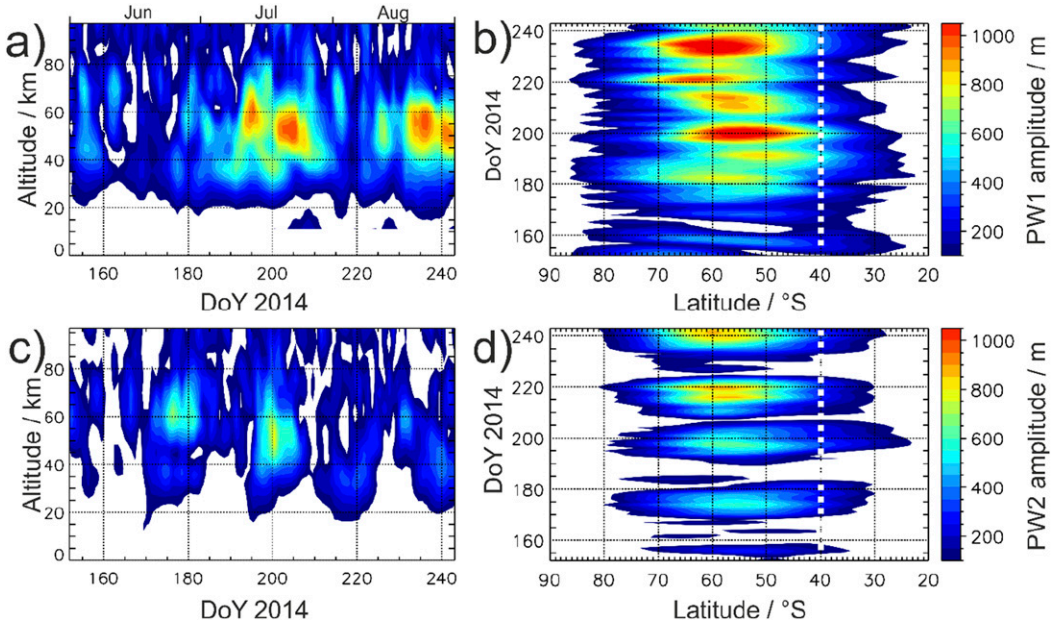

FIG. 11. Geopotential height amplitudes of stationary (a),(b) PW1 and (c),(d) PW2 as (left) a function of height and time averaged between 35° and 45°S and (right) a function of latitude and time averaged between 30- and 40-km altitude.

c. *Day-to-day variability over SI*

The day-to-day variability of the atmospheric conditions for an area encompassing the SI of New Zealand is shown by altitude–time sections derived from the operational IFS analyses in Fig. 3. The tropospheric properties and the variability of wind and temperature have already been discussed in the previous sections. Here, we concentrate on the stratospheric conditions. In general, upper-stratospheric and mesospheric winds were large with $V_H > 80\,\mathrm{m\,s^{-1}}$ from June until the middle of July 2014 (Fig. 3a). As expected for the PNJ, the main wind direction was westerly. In mid-July, winds turned slightly to southwesterly and became significantly weaker as a result of the displaced polar vortex and the associated southward migration of the PNJ (Fig. 3b). In August 2014, the weaker stratospheric winds varied considerably and the PNJ returned for only a few days. In the lower and middle stratosphere (<30-km altitude) horizontal winds were often smaller than $20\,\mathrm{m\,s^{-1}}$. Only during a few episodes was the stratospheric wind speed enhanced.

The dominant feature of the temperature evolution is the variability of the warm stratopause layer at around 50-km altitude (Fig. 3c). The descent and broadening of the stratopause in the middle to end of July 2014 occurred with the amplifying planetary wave amplitude (cf. the amplitudes of PW1 and PW2 around day 200 in Fig. 11). At the same time the EP-flux divergence (convergence) was maximized over New Zealand (toward the equator) between 40- and 50-km altitude (not shown). This can explain the descent and adiabatic warming of the stratopause region (see also description in section 5b). In the middle and lower stratosphere, episodes of $T < 200\,\mathrm{K}$ only occurred sporadically when the cold pool of the polar vortex extended north over New Zealand (Fig. 3c). Appendix B documents that the stratospheric temperatures from the ECMWF IFS are reliable up to an altitude of about 60 km. There, we compared the IFS data with the Rayleigh lidar observations by TELMA at Lauder. Although the profiles are compared only for a single location on New Zealand, the quantitative agreement indicates that essential features of the thermal structure of the atmosphere up to the stratopause are captured quantitatively well.

d. *High-altitude NAVGEM reanalyses*

ECMWF IFS analyses are progressively impacted by increased numerical damping above 60-km altitude and do not contain tides, which constitute the dominant mode of variability in the MLT region from ~60 to 100 km (Oberheide et al. 2015), where many key DEEPWAVE measurements took place (Fritts et al. 2016). Accordingly, a series of high-altitude reanalyses were performed for the DEEPWAVE austral winter using a research NAVGEM configuration (Eckermann et al. 2016). Figure 13 displays time series of reanalyzed NAVGEM temperature T, horizontal wind speed V_H,

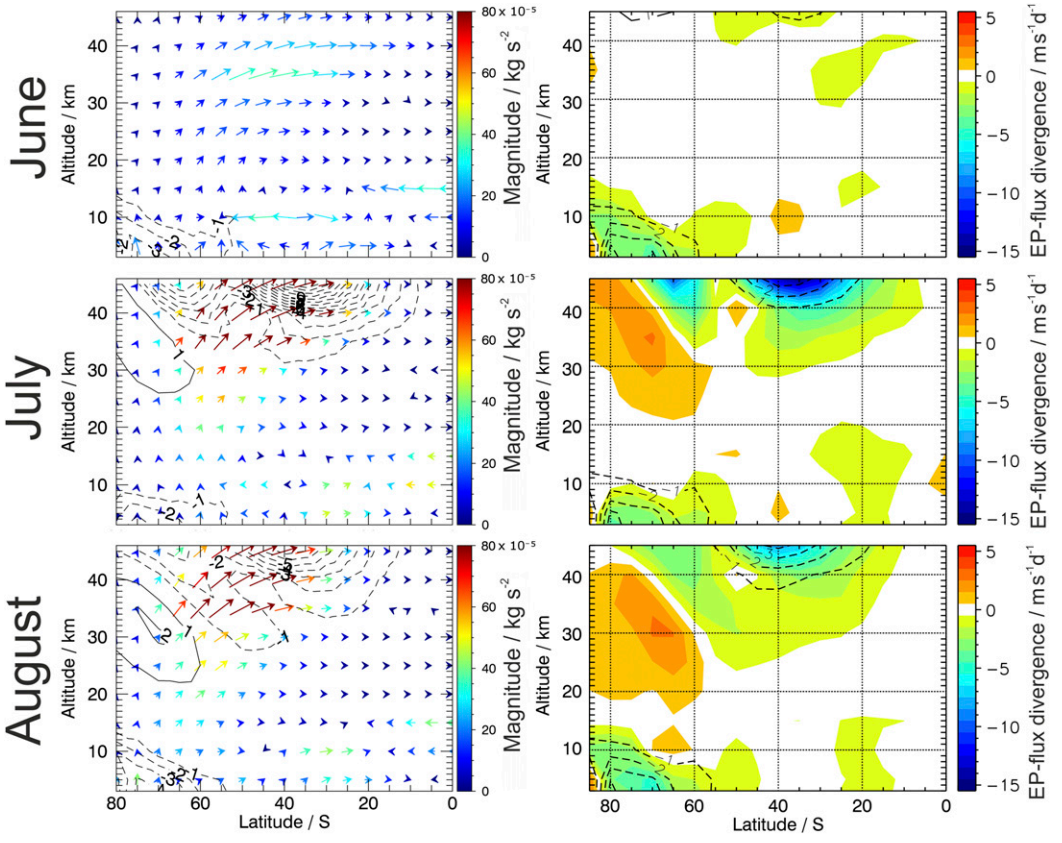

FIG. 12. (left) EP flux vectors **F** (arrows) and divergence $\nabla \cdot \mathbf{F}$ [black contour lines, dashed: negative values (i.e., convergence)] as monthly mean for JJA 2014 of ERA-Interim data. (right) EP flux divergence $\nabla \cdot \mathbf{F}$ as monthly mean for JJA 2014 of ERA-I data (color coded) and climatological mean from 37 years's worth of ERA-Interim data [black contour lines, dashed: negative values (i.e., convergence)]. The EP-flux vectors (F_ϕ, F_z) are scaled as $(p_0/p)^{1/2}(F_\phi, 100F_z)$. Note that the lengths of the vectors are plotted relative to the corresponding largest magnitude for each month. So the length gives an impression of the direction and relative magnitude for each month, while the color coding of the arrows allows a direct comparison of the three months.

and wind direction α_H over the New Zealand region (40°–50°S and 165°E–180°) during the 2014 austral winter, with separate panels depicting layer averages for the upper stratosphere (10–1 hPa), the lower mesosphere (1–0.1 hPa), the upper mesosphere (0.1–0.01 hPa), and the lower thermosphere (0.01–0.001 hPa). These time series have an hourly resolution, with the 6-hourly reanalysis fields interspersed with 1–5-h forecasts initialized from each successive reanalysis. The data series of temperature and wind can be decomposed into background (X_0), tides, and gravity wave perturbations (Hoffmann et al. 2010). For the background a 4-day running mean was used. This background together with the respective standard deviation, representing tides and gravity wave perturbations, is also shown in Fig. 13. Increasing short-term variability with altitude reflects progressively increasing tidal amplitudes, most notably a large-amplitude migrating semidiurnal tide in the mid-latitude MLT [Eckermann et al. (2016) and appendix D].

The evolution of background V_H and T in the upper stratosphere (Fig. 13a) is similar to the result discussed with respect to the ECMWF IFS data (Fig. 3). Westerly winds of about $V_H \approx 80\,\mathrm{m\,s^{-1}}$ and $T \approx 220\,\mathrm{K}$ fluctuated weakly until mid-July 2014. Because of the planetary waves and the associated displacement of the polar vortex occurring in the middle of July, the magnitude of V_H dropped by a factor of about 2, T increased, and wind directions became more variable. As expected for the stratopause layer, wind and temperature were maximized between 1 and 0.1 hPa (~50–65 km), attaining values of $V_H \geq 100\,\mathrm{m\,s^{-1}}$ and $T \approx 250\,\mathrm{K}$, respectively (Fig. 13b). In the upper mesosphere and lower thermosphere, V_H and T are generally lower (Figs. 13c,d). As in the layer below, the winds weakened and changed direction with enhanced fluctuations in the upper mesosphere in August (Fig. 13c). The onset of weakening winds varied in the respective layers. While V_H in the mesosphere (Figs. 13b,c) had weakened by 15 July 2014,

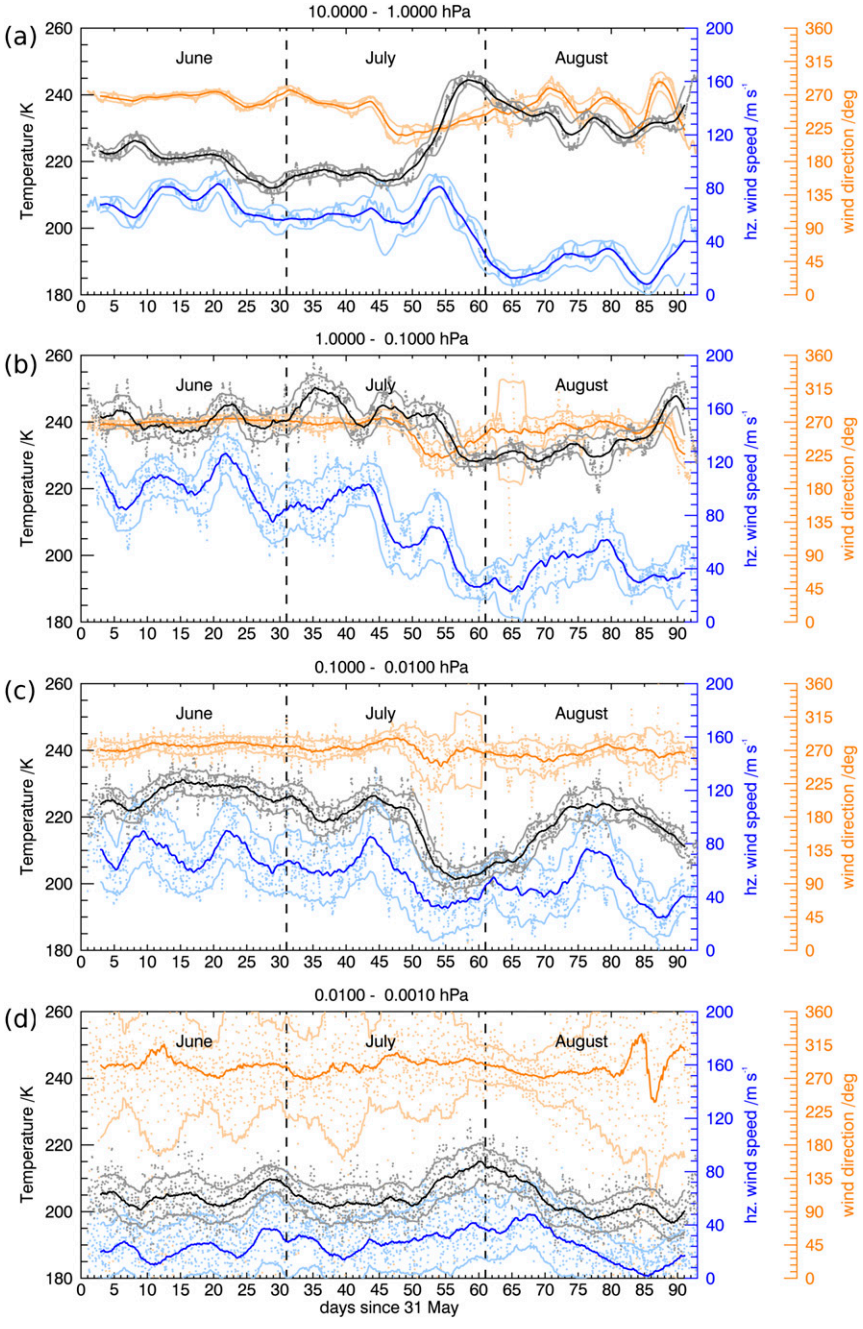

FIG. 13. NAVGEM T119L74 6-hourly analysis and 1-hourly forecasts averaged over the area between 40°–50°S and 165°E–180° of 4-day running mean (X_0) temperature (black) and horizontal wind speed (blue) and wind direction (orange) as layer averages taken between (a) 10 and 1, (b) 1 and 0.1, (c) 0.1 and 0.01, and (d) 0.01 and 0.001 hPa. Full data (X_0 + perturbations + tides) are shown as light-colored dots and the standard deviation with respect to X_0 as light-colored solid lines.

the gradual reduction in the upper stratosphere (Fig. 13a) began around 5 days later, then dropped to ~10–20 m s^{-1} in early August and stayed weak throughout August compared to June and July. Interestingly, tidal fluctuations seem to be noticeably reduced around the end of July and beginning of August in the lower thermosphere (see Fig. 13d). During the shift of the polar vortex, the increase in temperature in the upper stratosphere (Fig. 13a) was accompanied by increasing temperatures in the lower thermosphere (Fig. 13d)

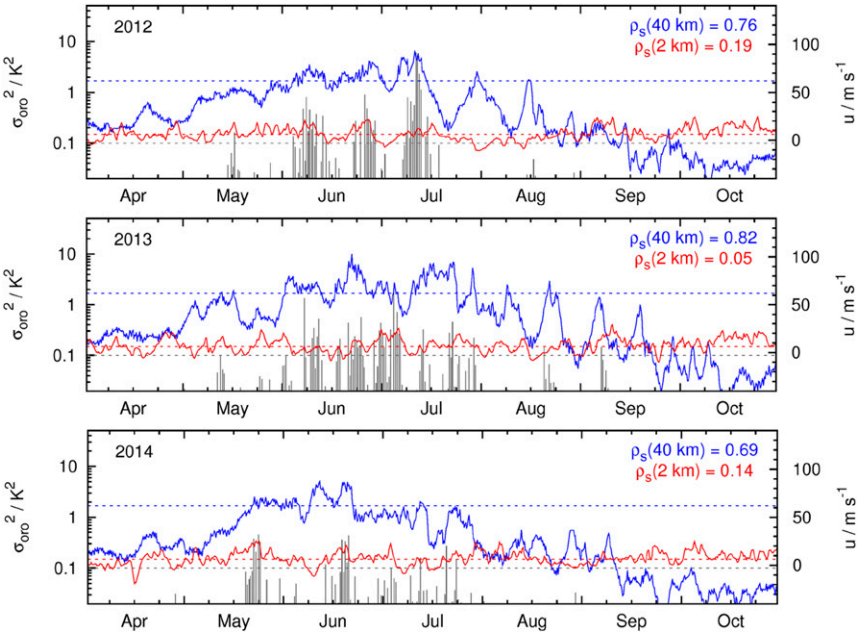

FIG. 14. Time series of AIRS 4.3-μm brightness temperature variance differences (gray) and ERA-Interim zonal winds at 2-km (red) and 40-km (blue) log-pressure altitude from 1 Apr to 31 Oct (top) 2012, (middle) 2013, and (bottom) 2014 in NZ. Gray dotted lines indicate the 0.1-K^2 threshold used to detect orographic gravity waves. The red and blue dotted lines depict zonal wind levels of 6 and 64 m s^{-1} used to predict mountain wave events in the AIRS observations. The values of u are area averages covering 48°–40°S, 166.5°–176.5°E and refer to the AIRS observational level (3 hPa, about 40 km) and the low level (750 hPa, about 2 km).

starting on 20 July. Decreasing temperatures are found in the mesosphere starting in the upper mesosphere on 20 July (Fig. 13c) and about 5 days later in the lower mesosphere (Fig. 13b).

It is worth mentioning here that the NAVGEM and ECMWF IFS analyses and forecasts are in good quantitative agreement up to about 1 hPa (approximately 50 km). The effect of the lower spatial resolution of NAVGEM compared to ECMWF is not relevant since the data used are averaged over a large area. A plot of the temporal evolution for T, V_H, and α_H from the IFS at 10–1 hPa is identical to Fig. 13a (not shown). Differences between NAVGEM and the IFS were found at higher altitudes because of the numerical damping in the uppermost layers of the IFS (see appendix B).

6. SI of New Zealand: A hotspot of orographic gravity waves in the stratosphere in 2014?

Recently, Hoffmann et al. (2016) conducted a comprehensive analysis of the stratospheric gravity wave activity at Southern Hemispheric hotspots using AIRS data. They found New Zealand being 1 of 18 hotspots. The stratospheric gravity wave occurrence frequency, being the fraction of AIRS overpasses showing gravity wave activity compared to the total number of overpasses, was 14% for New Zealand in the months of April–October from 2003 to 2014 [Table 1 in Hoffmann et al. (2016)]. Using a two-box method and employing a threshold for the observed brightness temperature variance of $\sigma^2_{\text{oro}} = 0.1\,\text{K}^2$, the occurrence frequency f_{oro} of orographic gravity waves above New Zealand was determined to be 9%; that is, most of the detected stratospheric gravity waves (about 70%) originate from the flow past the Southern Alps. Figure 14 shows the time series of the orographic gravity wave variances σ^2_{oro} based on individual AIRS overpasses and, in addition, the ERA-Interim background zonal wind u at different height levels above the New Zealand SI for the years 2012–14.

First of all, orographic gravity wave variances of all three years as seen by AIRS are largest and most frequent in May–July (i.e., the period chosen for the DEEPWAVE field phase). An interesting side note is that the rise above the threshold of 6 m s^{-1} for low-level winds in spring (September–October) confirms the extensive experience of glider pilots that favorable wave flight conditions occur during this season (R. Heise 2015, personal communication; B. Liley 2014, personal communication). However, the stratospheric zonal winds are weak and even westward during this period (September–October) and likely prevent deep vertical propagation.

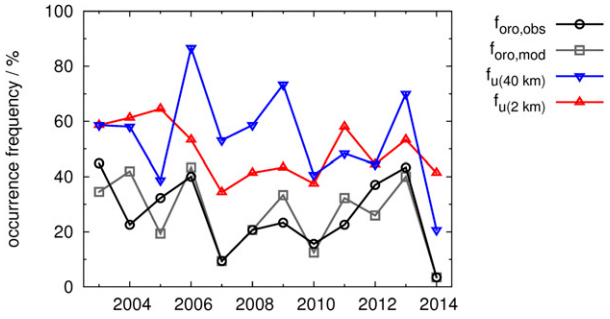

FIG. 15. Yearly variability of inferred orographic wave activity over NZ during June–July for the years 2003–14. Time series show occurrence frequencies of orographic waves from AIRS observations (black) and a simple mountain wave prediction model of Hoffmann et al. (2016) (gray). Also shown are occurrence frequencies of the zonal winds at 2-km (red) and 40-km (blue) altitude exceeding the prediction model thresholds, which are 6 and 64 m s^{-1}, respectively.

The Spearman rank-order correlation coefficient ρ_s between σ^2_{oro} and U is generally low at low levels, with ρ_s (2 km) ranging from 0.05 to 0.19. The correlation coefficient is high for the zonal wind at the observational level, with ρ_s (40 km) ranging from 0.69 to 0.82. This means that the AIRS observations are more strongly influenced by the observational filter, which is controlled by the background wind at the height level of the observations influencing the waves' vertical wavelength, than by the orographic forcing itself. Therefore, the weaker orographic wave activity in the stratosphere during the year 2014 compared to the years 2012 and 2013 applies for the wave activity seen by AIRS, which does not solely depend on the low-level wind but mainly on the stratospheric wind. During July and August 2014, the polar vortex was displaced toward South America as a result of the enhanced PW activity causing weaker winds in the stratosphere in the vicinity of New Zealand. In addition low-level forcing was influenced by southwesterly flows and blocking situations (see section 3). Therefore, the orographic gravity waves observed and predicted by the simple model, as in Hoffmann et al. (2016), show a pronounced 12-yr minimum (Fig. 15). Again this is all valid for orographic wave activity in the observational range of AIRS and identified by the analysis method of Hoffmann et al. (2016).

7. Summary

We have presented a comprehensive analysis of the prevailing atmospheric conditions relative to climatology of the atmosphere from the ground to the lower thermosphere over the New Zealand region during the 2014 austral winter. Our study employs various observations, analyses, and reanalyses. The results give first insights into the relationship between the prevailing atmospheric conditions and observed gravity wave activity during the DEEPWAVE field campaign and serve as a reference for future investigations of specific gravity wave events observed during DEEPWAVE. The main results of our analysis can be summarized as follows.

Local tropospheric climatological indices (SOI and SAO) suggest a tendency for southwesterly flows and blocking over New Zealand during DEEPWAVE. A classification of the tropospheric flow regimes according to Kidson (2000) and Renwick (2011) revealed that the blocking regimes, with an occurrence frequency of 36%, and the SW regime, with a frequency of about 18%, were the most frequent ones that occurred during JJA 2014. Compared to the values found by Renwick (2011) for JJA of 1958–2010, the occurrence frequency was twice as high in JJA 2014 for the HSE regime (21.7% vs 10.6%) and enhanced for the SW regime (17.9% vs 11.3%). Altogether, the trough group regimes were underrepresented compared to results from the 40-yr climatology of Kidson (2000). Many DEEPWAVE aircraft mountain wave missions were conducted during the TNW regime. On 5 out of 7 days, when the TNW regime occurred in June and July 2014, aircraft missions were devoted to observe deep propagating orographic gravity waves and in the majority of cases significant and strong mountain wave activity was found (Table 1). During the flight planning process, the weak cross-mountain wind component at 700 hPa occurring during the SW regimes caused only weak forcing conditions, which often disqualified mountain waves as primary targets for selected missions. For IOPs 6 and 10, which were conducted during the SW regimes, moderate and even strong mountain wave activity was reported at flight level and also in the MLT.

The tropopause height fluctuated between 8 and 13 km during JJA 2014. The TIL was a dominant feature of the UTLS during the DEEPWAVE period but varied markedly in strength and depth (Fig. 4a). This variability can be related to the alternating appearance of anticyclones and cyclones over New Zealand, given that "anticyclones are characterized by a distinct peak in N^2 right above the tropopause" (Wirth 2003, 2004). A simplified reflection coefficient for hydrostatic gravity waves was calculated for JJA 2014 using both the representative buoyancy frequencies N_T and N_S from the troposphere and stratosphere and maximum values N_{MAX} attained within the TIL. The approximated hydrostatic reflection coefficient showed significant enhancement from reaching up to 0.6 when the N^2 peak of the TIL was taken into account. A reflection coefficient of $r \geq 0.5$ was associated with a reduction of the vertical energy flux between 4- and 12-km altitude simulated by WRF and suggests significant partial reflection of vertically propagating gravity waves at the tropopause. These

findings may point to another reason for the reported moderate and strong gravity wave activity during the SW regime. The TIL is relatively weak and the hydrostatic reflection coefficient is close to 0.4 for this regime (e.g., 19 and 20 June and 4 July in Fig. 5a) because of the influence of the cyclone located SE of New Zealand.

In accordance with the climatology, the STJ was the dominant tropopause jet within the DEEPWAVE region and period. A double-jet structure consisting of STJ to the north and PFJ to the south was present on nearly all days in July and August 2014. The analysis of the positions and strengths of both jets revealed that the STJ was located in the vicinity of New Zealand (e.g., south of 35°S at 169°E), most often in June, while the PFJ was located in the vicinity of New Zealand (e.g., north of 52°S at 169°E) most often in July (Fig. 6b). For the IOPs when the STJ was involved, stronger forcing conditions occurred than in cases when the PFJ was present. During aircraft missions under stronger forcing conditions of the STJ, wave breaking and turbulence were reported [see Table 4 in Fritts et al. (2016)]. For cases when the PFJ was located close to the SI, weak mountain wave activity at flight level was reported. Surprisingly, strong mountain wave activity in the stratosphere and the MLT were reported for those cases. Based on these findings, we hypothesize that breaking in the UTLS was strongly related to the STJ affecting the propagation through the UTLS while the PFJ was the main driver when weak forcing in the troposphere and large amplitudes in the MLT were observed.

The evolution of wind and thermal conditions in the middle atmosphere above New Zealand during the DEEPWAVE campaign can be summarized as follows. Until about the middle of July 2014, the PNJ was located above the SI with strong westerly winds ($V_H > 100\,\mathrm{m\,s^{-1}}$) covering an altitude range from about 40 to 70 km. Afterward, the upper-level winds above SI weakened and changed direction from westerly to more southerly. The stratospheric winds in the vicinity of New Zealand were up to $10\,\mathrm{m\,s^{-1}}$ weaker in July and August 2014 than the climatological means. Planetary wave analysis of PW1 and PW2 amplitudes and EP flux revealed that this transition was triggered by planetary waves, which caused a southward displacement of the PNJ. Afterward, the background conditions in the middle atmosphere changed and were characterized by much weaker and more variable winds from the middle of July to the end of August 2014. Together with the EP-flux convergence and the enhanced PW activity, the stratopause over the NZ region descended and broadened, causing a warming of the upper stratosphere, a cooling in the mesosphere, and a warming of the lower thermosphere.

AIRS satellite observations in the upper stratosphere using the new method of Hoffmann et al. (2016) revealed that orographic gravity wave variances for 2014 were largest and most frequent in May–July (i.e., the period of the DEEPWAVE field phase). However, those analyses also showed that there was a pronounced 12-yr minimum in 2014 with respect to the orographic gravity wave activity in the observational range of AIRS, which depends not only on the low-level winds but mainly on the stratospheric winds.

Acknowledgments. Part of this research was funded by the German research initiative ''Role of the Middle Atmosphere in Climate'' (ROMIC/01LG1206A) funded by the German Ministry of Research and Education in the project ''Investigation of the Life Cycle of Gravity Waves'' (GW-LCYCLE), and by the Deutsche Forschungsgemeinschaft (DFG) via the Project MS-GWaves (GW-TP/DO 1020/9-1 and PACOG/RA 1400/6-1). The NRL components of this research were supported by the Chief of Naval Research through the NRL Base Program (PE 0601153N). Access to the ECMWF data was possible through the special project ''HALO Mission Support System.'' We thank the NASA/Jet Propulsion Laboratory for providing access to the *Aura*/MLS level 2 retrieval products available online (http://mirador.gsfc.nasa.gov). NCEP–NCAR reanalysis data were provided by the NOAA/OAR/ESRL PSD, Boulder, Colorado, and downloaded from their Web site (http://www.esrl.noaa.gov/psd/). AIRS data products are distributed by the NASA Goddard Earth Sciences Data Information and Services Center (GES DISC). Objective tropospheric regime classification was provided by NIWA. We sincerely thank all three anonymous reviewers for their valuable comments and suggestions, which led the manuscript to its present state.

APPENDIX A

Key Acronyms Used in This Paper

AAO	Antarctic Oscillation
AIRS	Atmospheric Infrared Sounder
DEEPWAVE	Deep Propagating Gravity Wave Experiment
ECMWF	European Centre for Medium-Range Weather Forecasts
EP	Eliassen–Palm
ERA	ECMWF Re-Analysis
FF	research flight Falcon
GB	ground-based measurement
GV	Gulfstream 5 research aircraft
GW	gravity wave

IFS	Integrated Forecast System
IOP	intensive observing period
JJA	June–August
MLS	Microwave Limb Sounder
MLT	mesosphere and lower thermosphere
MSLP	mean sea level pressure
MW	mountain wave
NAVGEM	Navy Global Environmental Model
NCAR	National Center for Atmospheric Research
NCEP	National Centers for Environmental Prediction
NSF	National Science Foundation
NZ	New Zealand
PF	predictability flight
PFJ	polar front jet
PNJ	polar night jet
PW1 and PW2	planetary wave with zonal wavenumbers 1 and 2
RF	research flight GV
SABER	Sounding of the Atmosphere Using Broadband Emission Radiometry
SAM	southern annular mode
SAO	semiannual oscillation
SH	Southern Hemisphere
SI	South Island
SO	Southern Ocean
SOI	Southern Oscillation index
STJ	subtropical jet
TELMA	Temperature Lidar for Middle Atmosphere Research
TIL	tropopause inversion layer
TW	trailing wave
UTLS	upper troposphere–lower stratosphere
WRF	Weather Research and Forecasting Model

Weather Regimes for New Zealand

H, HNW, and W	zonal group: high, high northwest, and westerly flow
T, SW, TNW, and TSW	trough group: trough, southwesterly flow, trough northwest, and trough southwest
HSE, HE, NE, HW, and R	blocking group: high southeast, high east, northeasterly flow, high west, and ridge over New Zealand

APPENDIX B

Lidar Temperature Measurements and ECMWF IFS

Figure B1 shows TELMA temperature measurements over Lauder from the end of June to November 2014. The TELMA data have effective temporal and vertical resolutions of 60 min and 2900 m, respectively. In the beginning of July the stratopause is located between 50- and 60-km altitude with stratopause temperatures around 260 K. At the end of July the stratopause altitude decreases suddenly down to 40–50-km altitude; however, stratopause temperatures stay approximately the same. Around the middle of August 2014, the stratopause is highly distorted and stratopause temperatures are reduced. During end of August, a stable and warm stratopause forms around 50-km altitude, with temperatures of ≈270 K. Toward November, the stratopause temperature increases gradually.

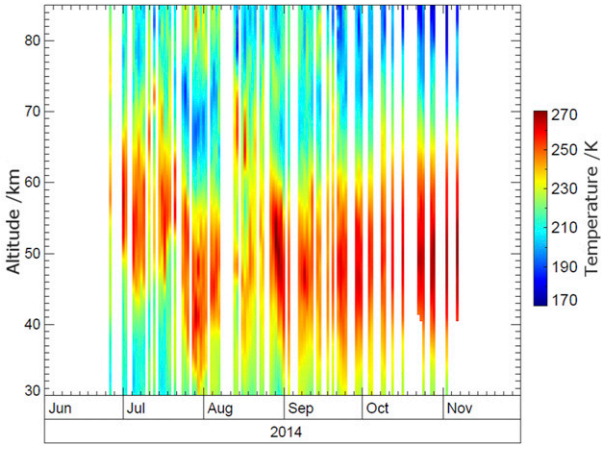

FIG. B1. Temperature measurements by TELMA above Lauder, during SH winter 2014. The temperature data have an effective temporal and vertical resolution of 60 min × 2900 m.

The left panel of Fig. B2 depicts the mean lidar temperature at Lauder between July and September 2014 (black line) in comparison to the ECMWF temperature at Lauder (blue line). We limit the comparison to the period July–September as the data coverage by the lidar is very high during this period (cf. Fig. B1). Note that for comparison ECMWF data were only taken at times when lidar data were available as well. The lidar temperature exhibits a mean stratopause height of ≈48 km with a stratopause temperature of 247 K, and in the mesosphere the temperature decreases with altitude, reaching 215 K at 70-km altitude. The ECMWF IFS 40r1 cycle exhibits a higher and colder stratopause (52 km and 245 K) than the lidar measurements, and in the mesosphere temperatures decrease rapidly with increasing altitude, reaching 200 K at 70-km altitude. Between 30- and 34-km altitude, lidar temperatures are on average lower than ECMWF temperatures. Note that lidar temperatures in this altitude region might be low biased as a result of the presence of stratospheric aerosols. Thus, we refrain from interpreting this altitude region.

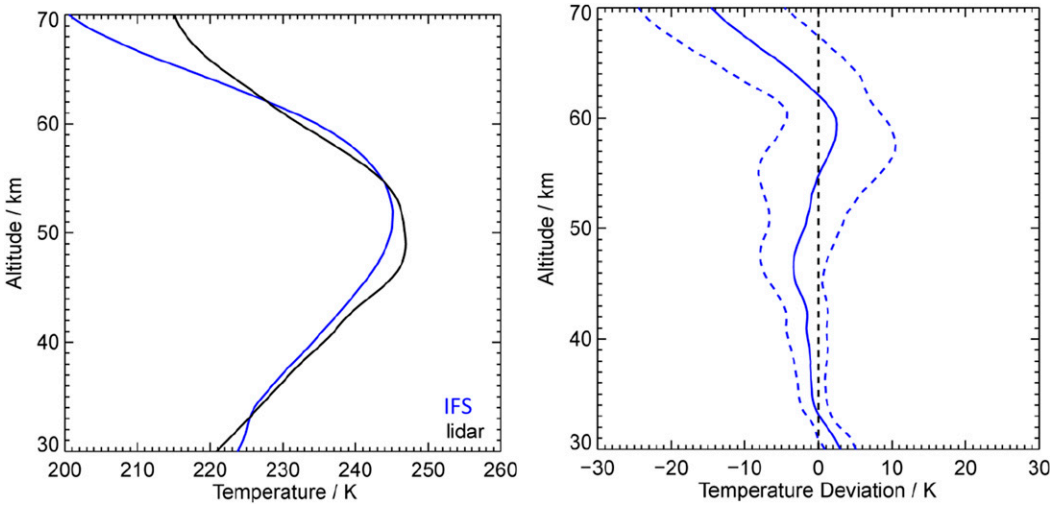

FIG. B2. (left) Mean temperature profile observed by TELMA (black line) and analyzed by ECMWF IFS cycle 40r1 (blue line) above Lauder, from July to September 2014. (right) Resulting mean temperature deviation between the lidar and the ECMWF IFS (solid) plus the standard deviation from the mean (dashed lines). For this comparison ECMWF data were only taken at times when lidar data were available. Both datasets were interpolated onto the same altitude grid with a resolution of 500 m.

The deviation between the ECMWF IFS cycle 40r1 temperature and the lidar temperature (Fig. B2, right panel) shows that ECMWF temperatures are 1–3 K lower than the lidar temperatures between 34- and 54-km altitude. At 60-km altitude, ECMWF temperatures are 2 K warmer than the lidar temperatures, corresponding to the higher stratopause in ECMWF. Above 60-km altitude the temperature deviation decreases rapidly with increasing altitude, resulting in ECMWF temperatures being 15 K lower than the lidar temperatures at 70-km altitude. Standard deviations of the temperature deviation are small in the stratosphere (≈3 K) and increase up to 10 K in the mesosphere. Note that the temperature deviation profile at Lauder is very similar to the one published by Le Pichon et al. (2015, their Fig. 4) for a Northern Hemisphere midlatitude site [Haute de Provence Observatory in southeast France (43.9°N, 5.7°E)]. The temperatures of the ECMWF IFS cycle 40r1 agree well with the lidar observations up to 60-km altitude. This is the same altitude up to which good agreement was also found for wind data by Le Pichon et al. (2015). Thus, we regard the ECMWF dataset as a good indicator for the mean dynamical state of the atmosphere up to 60-km altitude.

APPENDIX C

Planetary Waves in ERA-Interim

Figure C1 is similar to Fig. 10 but is derived from ERA-Interim data (i.e., the vertical profiles of the monthly means of PW1 and PW2 geopotential height amplitude). Comparing these two figures reveals very good agreement between the amplitude of the PWs derived from MLS and from ERA-Interim in the stratosphere. An advantage of MLS and the cause for its usage is the much higher altitude range of MLS compared to ERA-Interim. Since the DEEPWAVE

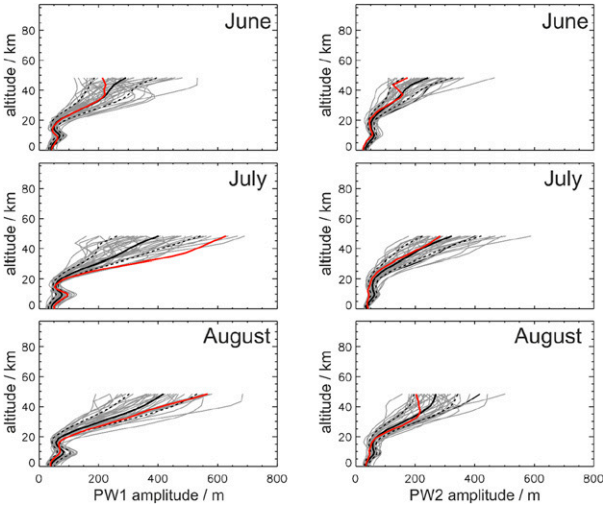

FIG. C1. Vertical profiles of the monthly means of stationary PW1 and PW2 amplitudes zonally averaged between 30° and 50°S from ERA-Interim for JJA. Thin gray lines represent the means from the 37 available years. Solid black lines are the long-term averages and their respective standard deviations are plotted by dashed lines. The red lines represent the monthly means for the DEEPWAVE during 2014. Axes are the same as for MLS in Fig. 10.

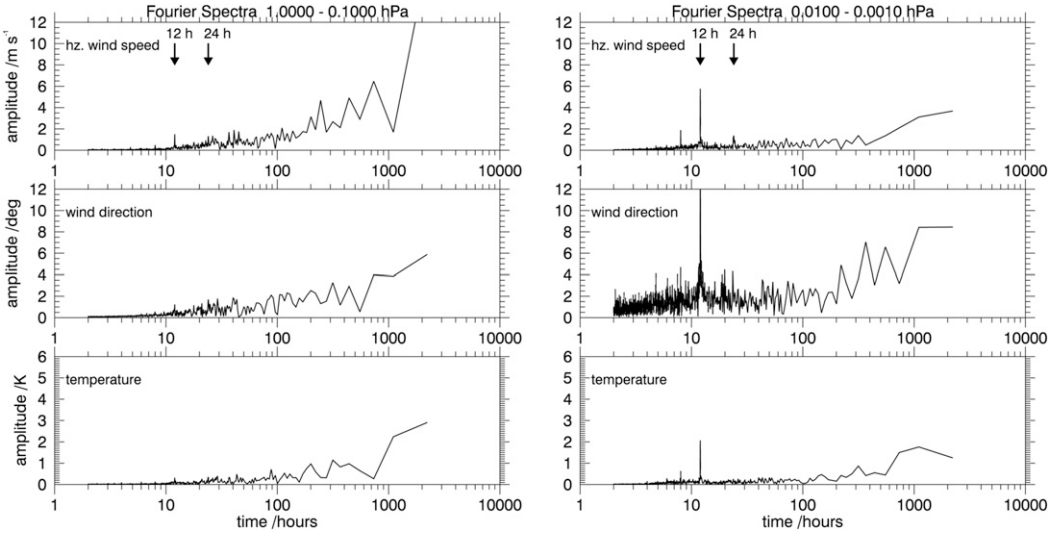

FIG. D1. Fourier spectra of NAVGEM (top) horizontal wind, (middle) wind direction, and (bottom) temperature in the (left) lower mesosphere and (right) lower thermosphere.

campaign also includes mesospheric measurements (e.g., Kaifler et al. 2017), it is reasonable to consider PW not only in the stratosphere but also in the mesosphere because of the potential interactions of GWs with PWs.

APPENDIX D

Semidiurnal Tides in NAVGEM

Fourier spectra of NAVGEM wind and temperature data show the increasing influence of the semidiurnal tide with altitude (Fig. D1).

REFERENCES

Alexander, M. J., 1998: Interpretations of observed climatological patterns in stratospheric gravity wave variance. *J. Geophys. Res.*, **103**, 8627–8640, https://doi.org/10.1029/97JD03325.

Andrews, D. G., J. R. Holton, and C. B. Leovy, 1987: *Middle Atmosphere Dynamics.* Academic Press, 489 pp.

Aumann, H. H., and Coauthors, 2003: AIRS/AMSU/HSB on Aqua mission: Design, science objectives, data products, and processing systems. *IEEE Trans. Geosci. Remote Sens.*, **41**, 253–264, https://doi.org/10.1109/TGRS.2002.808356.

Baines, P. G., 1995: *Topographic Effects in Stratified Flows*. 1st ed. Cambridge University Press, 482 pp.

Birner, T., 2006: Fine-scale structure of the extratropical tropopause region. *J. Geophys. Res.*, **111**, D04104, https://doi.org/10.1029/2005JD006301.

——, A. Dörnbrack, and U. Schumann, 2002: How sharp is the tropopause at midlatitudes? *Geophys. Res. Lett.*, **29**, 1700, https://doi.org/10.1029/2002GL015142.

Bossert, K., and Coauthors, 2015: Momentum flux estimates accompanying multiscale gravity waves over Mount Cook, New Zealand, on 13 July 2014 during the DEEPWAVE campaign. *J. Geophys. Res. Atmos.*, **120**, 9323–9337, https://doi.org/10.1002/2015JD023197.

Burnett, A. W., and A. R. McNicoll, 2000: Interannual variations in the Southern Hemisphere winter circumpolar cortex: Relationships with the semiannual oscillation. *J. Climate*, **13**, 991–999, https://doi.org/10.1175/1520-0442(2000)013<0991:IVITSH>2.0.CO;2.

Chahine, M. T., and Coauthors, 2006: AIRS: Improving weather forecasting and providing new data on greenhouse gases. *Bull. Amer. Meteor. Soc.*, **87**, 911–926, https://doi.org/10.1175/BAMS-87-7-911.

Dee, D. P, and Coauthors, 2011: The ERA-Interim reanalysis: Configuration and performance of the data assimilation system. *Quart. J. Roy. Meteor. Soc.*, **137**, 553–597, https://doi.org/10.1002/qj.828.

Dunkerton, T., 1978: On the mean meridional mass motions of the stratosphere and mesosphere. *J. Atmos. Sci.*, **35**, 2325–2333, https://doi.org/10.1175/1520-0469(1978)035<2325:OTMMMM>2.0.CO;2.

——, C.-P. F. Hsu, and M. E. McIntyre, 1981: Some Eulerian and Lagrangian diagnostics for a model stratospheric warming. *J. Atmos. Sci.*, **38**, 819–843, https://doi.org/10.1175/1520-0469(1981)038<0819:SEALDF>2.0.CO;2.

Eckermann, S. D., and R. A. Vincent, 1993: VHF radar observations of gravity-wave production by cold fronts over southern Australia. *J. Atmos. Sci.*, **50**, 785–806, https://doi.org/10.1175/1520-0469(1993)050<0785:VROOGW>2.0.CO;2.

——, and Coauthors, 2016: Dynamics of orographic gravity waves observed in the mesosphere over the Auckland Islands during the Deep Propagating Gravity Wave Experiment (DEEPWAVE). *J. Atmos. Sci.*, **73**, 3855–3876, https://doi.org/10.1175/JAS-D-16-0059.1.

Ehard, B., and Coauthors, 2017: Horizontal propagation of large-amplitude mountain waves into the polar night jet. *J. Geophys. Res. Atmos.*, **122**, 1423–1436, https://doi.org/10.1002/2016JD025621.

Eliassen, A., and E. Palm, 1960: On the transfer of energy in stationary mountain waves. *Geophys. Publ.*, **22**, 1–23.

Fritts, D. C., and M. J. Alexander, 2003: Gravity wave dynamics and effects in the middle atmosphere. *Rev. Geophys.*, **41**, 1003, https://doi.org/10.1029/2001RG000106.

——, and Coauthors, 2016: The Deep Propagating Gravity Wave Experiment (DEEPWAVE): An airborne and ground-based exploration of gravity wave propagation and effects from their

sources throughout the lower and middle atmosphere. *Bull. Amer. Meteor. Soc.*, **97**, 425–453, https://doi.org/10.1175/BAMS-D-14-00269.1.

Gallego, D., P. Ribera, R. Garcia-Herrera, E. Hernandez, and L. Gimeno, 2005: A new look for the Southern Hemisphere jet stream. *Climate Dyn.*, **24**, 607–621, https://doi.org/10.1007/s00382-005-0006-7.

Gettelman, A., and T. Wang, 2015: Structural diagnostics of the tropopause inversion layer and its evolution. *J. Geophys. Res. Atmos.*, **120**, 46–62, https://doi.org/10.1002/2014JD021846.

——, P. Hoor, L. L. Pan, W. J. Randel, M. I. Hegglin, and T. Birner, 2011: The extratropical upper troposphere and lower stratosphere. *Rev. Geophys.*, **49**, RG3003, https://doi.org/10.1029/2011RG000355.

Gill, A. E., 1982: *Atmosphere–Ocean Dynamics*. International Geophysics Series, Vol. 30, Academic Press, 662 pp.

Gong, D., and S. Wang, 1999: Definition of Antarctic Oscillation index. *Geophys. Res. Lett.*, **26**, 459–462, https://doi.org/10.1029/1999GL900003.

Gordon, N. D., 1986: The Southern Oscillation and New Zealand weather. *Mon. Wea. Rev.*, **114**, 371–387, https://doi.org/10.1175/1520-0493(1986)114<0371:TSOANZ>2.0.CO;2.

Grise, K. M., D. W. J. Thompson, and T. Birner, 2010: A global survey of static stability in the stratosphere and upper troposphere. *J. Climate*, **23**, 2275–2292, https://doi.org/10.1175/2009JCLI3369.1.

Hauchecorne, A., and M.-L. Chanin, 1980: Density and temperature profiles obtained by lidar between 35 and 70 km. *Geophys. Res. Lett.*, **7**, 565–568, https://doi.org/10.1029/GL007i008p00565.

Hoffmann, L., X. Xue, and M. J. Alexander, 2013: A global view of stratospheric gravity wave hotspots located with Atmospheric Infrared Sounder observations. *J. Geophys. Res. Atmos.*, **118**, 416–434, https://doi.org/10.1029/2012JD018658.

——, A. W. Grimsdell, and M. J. Alexander, 2016: Stratospheric gravity waves at Southern Hemisphere orographic hotspots: 2003–2014 AIRS/Aqua observations. *Atmos. Chem. Phys.*, **16**, 9381–9397, https://doi.org/10.5194/acp-16-9381-2016.

Hoffmann, P., E. Becker, W. Singer, and M. Placke, 2010: Seasonal variation of mesospheric waves at northern middle and high latitudes. *J. Atmos. Sol.-Terr. Phys.*, **72**, 1068–1079, https://doi.org/10.1016/j.jastp.2010.07.002.

Hogan, T. F., and Coauthors, 2014: The Navy Global Environmental Model. *Oceanography*, **27**, 116–125, https://doi.org/10.5670/oceanog.2014.73.

Jiang, J. H., S. D. Eckermann, D. L. Wu, and D.-Y. Wang, 2006: Interannual variation of gravity waves in the Arctic and Antarctic winter middle atmosphere. *Adv. Space Res.*, **38**, 2418–2423, https://doi.org/10.1016/j.asr.2005.09.036.

Kaifler, B., N. Kaifler, B. Ehard, A. Dörnbrack, M. Rapp, and D. C. Fritts, 2015: Influences of source conditions on mountain wave penetration into the stratosphere and mesosphere. *Geophys. Res. Lett.*, **42**, 9488–9494, https://doi.org/10.1002/2015GL066465.

Kaifler, N., B. Kaifler, B. Ehard, M. Rapp, R. Kivi, and B. Liley, 2017: Observational indications of downward-propagating gravity waves in middle atmosphere lidar data. *J. Atmos. Sol.-Terr. Phys.*, **162**, 16–27, https://doi.org/10.1016/j.jastp.2017.03.003.

Kalnay, E., and Coauthors, 1996: The NCEP/NCAR 40-Year Reanalysis Project. *Bull. Amer. Meteor. Soc.*, **77**, 437–471, https://doi.org/10.1175/1520-0477(1996)077<0437:TNYRP>2.0.CO;2.

Keller, T. L., 1994: Implications of the hydrostatic assumption on atmospheric gravity waves. *J. Atmos. Sci.*, **51**, 1915–1929, https://doi.org/10.1175/1520-0469(1994)051<1915:IOTHAO>2.0.CO;2.

Kidson, J. W., 2000: An analysis of New Zealand synoptic types and their use in defining weather regimes. *Int. J. Climatol.*, **20**, 299–316, https://doi.org/10.1002/(SICI)1097-0088(20000315)20:3<299::AID-JOC474>3.0.CO;2-B.

Kruse, C. G., and R. B. Smith, 2015: Gravity wave diagnostics and characteristics in mesoscale fields. *J. Atmos. Sci.*, **72**, 4372–4392, https://doi.org/10.1175/JAS-D-15-0079.1.

——, ——, and S. D. Eckermann, 2016: The midlatitude lower-stratospheric mountain wave "valve layer." *J. Atmos. Sci.*, **73**, 5081–5100, https://doi.org/10.1175/JAS-D-16-0173.1

Lait, L. R., 1994: An alternative form for potential vorticity. *J. Atmos. Sci.*, **51**, 1754–1759, https://doi.org/10.1175/1520-0469(1994)051<1754:AAFFPV>2.0.CO;2.

Le Pichon, R. S., and Coauthors, 2015: Comparison of co-located independent ground-based middle atmospheric wind and temperature measurements with numerical weather prediction models. *J. Geophys. Res. Atmos.*, **120**, 8318–8331, https://doi.org/10.1002/2015JD023273.

Lindzen, R. S., 1981: Turbulence and stress owing to gravity-wave and tidal breakdown. *J. Geophys. Res.*, **86**, 9707–9714, https://doi.org/10.1029/JC086iC10p09707.

Livesey, N. J., and Coauthors, 2017: EOS MLS version 4.2x level 2 data quality and description document. Jet Propulsion Laboratory Tech. Rep., California Institute of Technology, Pasadena, CA, 163 pp., https://mls.jpl.nasa.gov/data/v4-2_data_quality_document.pdf.

Manney, G., M. Hegglin, W. Daffer, M. Schwartz, M. Santee, and S. Pawson, 2014: Climatology of upper tropospheric/lower stratospheric (UTLS) jets and tropopauses in MERRA. *J. Climate*, **27**, 3248–3271, https://doi.org/10.1175/JCLI-D-13-00243.1.

Nappo, C. J., 2012: *An Introduction to Atmospheric Gravity Waves*. 2nd ed. Academic Press, 400 pp.

Oberheide, J., K. Shiokawa, S. Gurubaran, W. E. Ward, H. Fujiwara, M. J. Kosch, J. J. Makela, and H. Takahashi, 2015: The geospace response to variable inputs from the lower atmosphere: A review of the progress made by Task Group 4 of CAWSES-II. *Prog. Earth Planet. Sci.*, **2**, 1–31, https://doi.org/10.1186/s40645-014-0031-4.

Pautet, P.-D., and Coauthors, 2016: Large-amplitude mesospheric response to an orographic wave generated over the Southern Ocean Auckland Islands (50.7°S) during the DEEPWAVE project. *J. Geophys. Res. Atmos.*, **121**, 1431–1441, https://doi.org/10.1002/2015JD024336.

Plougonven, R., and F. Zhang, 2014: Internal gravity waves from atmospheric jets and fronts. *Rev. Geophys.*, **52**, 33–76, https://doi.org/10.1002/2012RG000419.

Renwick, J. A., 2011: Kidson's synoptic weather types and surface climate variability over New Zealand. *Wea. Climate*, **31**, 3–23.

Shaw, T., and J. Perlwitz, 2014: On the control of the residual circulation and stratospheric temperatures in the Arctic by planetary wave coupling. *J. Atmos. Sci.*, **71**, 195–206, https://doi.org/10.1175/JAS-D-13-0138.1.

Shibuya, R., K. Sato, Y. Tomikawa, M. Tsutsumi, and T. Sato, 2015: A study of multiple tropopause structures caused by inertia–gravity waves in the Antarctic. *J. Atmos. Sci.*, **72**, 2109–2130, https://doi.org/10.1175/JAS-D-14-0228.1.

Smith, R. B., 1979: The influence of mountains on the atmosphere. *Advances in Geophysics*, Vol. 21, Academic Press, 87–230, https://doi.org/10.1016/S0065-2687(08)60262-9.

——, and Coauthors, 2016: Stratospheric gravity wave fluxes and scales during DEEPWAVE. *J. Atmos. Sci.*, **73**, 2851–2869, https://doi.org/10.1175/JAS-D-15-0324.1.

Sutherland, B. R., 2010: *Internal Gravity Waves*. 1st ed. Cambridge University Press, 394 pp.

Taguchi, M., and D. L. Hartmann, 2006: Increased occurrence of stratospheric sudden warmings during El Niño as simulated by WACCM. *J. Climate*, **19**, 324–332, https://doi.org/10.1175/JCLI3655.1.

Trenberth, K. E., 1986: The signature of a blocking episode on the general circulation in the Southern Hemisphere. *J. Atmos. Sci.*, **43**, 2061–2069, https://doi.org/10.1175/1520-0469(1986)043<2061:TSOABE>2.0.CO;2.

Waters, J., and Coauthors, 2006: The Earth Observing System Microwave Limb Sounder (EOS MLS) on the Aura satellite. *IEEE Trans. Geosci. Remote Sens.*, **44**, 1075–1092, https://doi.org/10.1109/TGRS.2006.873771.

Wirth, V., 2003: Static stability in the extratropical tropopause region. *J. Atmos. Sci.*, **60**, 1395–1409, https://doi.org/10.1175/1520-0469(2003)060<1395:SSITET>2.0.CO;2.

——, 2004: A dynamical mechanism for tropopause sharpening. *Meteor. Z.*, **13**, 477–484, https://doi.org/10.1127/0941-2948/2004/0013-0477.

WMO, 1957: Meteorology—A three-dimensional science. *WMO Bull.*, **6**, 134–138.

Wu, D. L., P. B. Hays, and W. R. Skinner, 1995: A least squares method for spectral analysis of space-time series. *J. Atmos. Sci.*, **52**, 3501–3511, https://doi.org/10.1175/1520-0469(1995)052<3501:ALSMFS>2.0.CO;2.

——, P. Preusse, S. D. Eckermann, J. H. Jiang, M. de la Torre Juarez, L. Coy, B. Lawrence, and D. Y. Wang, 2006: Remote sounding of atmospheric gravity waves with satellite limb and nadir techniques. *Adv. Space Res.*, **37**, 2269–2277, https://doi.org/10.1016/j.asr.2005.07.031.